Targeting the Innate Immune System Using Protein Design

Chloe Shellanne Adams

A dissertation

submitted in partial fulfillment of the

requirements for the degree of

Doctor of Philosophy

University of Washington

2024

Reading Committee:

Neil King, Chair

Daniel Stetson

Frank DiMaio

Program Authorized to Offer Degree:

Biochemistry

University of Washington

Abstract

Targeting the Innate Immune System Using Protein Design

Chloe Shellanne Adams

Chair of the Supervisory Committee:

Neil King

Department of Biochemistry

Subunit vaccines require adjuvants to create a robust immune response. Adjuvants are limited by formulation difficulties and the types of immune responses they elicit. There is a need for a new generation of adjuvants. An ideal adjuvant would be easy to characterize with a protein antigen, hyperstable, specific to a defined immune pathway, and easily modified. In this thesis, I describe the application of protein design to create protein based adjuvants. We created novel minibinders that can be linked together to agonize TLR3. Additional stories are presented which describe the efforts to create protein binders for TLR5, TREM-2, and FcγRIIA.

Table of Contents

Acknowledgements

This dissertation was completed in the lab of Dr. Neil King, who is a relentlessly optimistic mentor and person. Thank you Neil for talking to me about everything from Kansas City Chiefs to symmetry to assay design. You had unwavering faith in the projects described here- even when I did not. I would also like to thank my committee members for their advice over the years- Dr. Dan Stetson, Dr. Frank Dimaio, Dr. David Baker, and Dr. Kim Woodrow.

I would like to acknowledge my scientific mentors before grad school, Dr. Brian Ackley and Dr. Dana Tucker, for teaching me what research was and encouraging me to pursue my PhD. Brian was the only professor to give me a chance as an undergraduate researcher and was incredibly supportive and patient. When I pursued biochemistry instead of neurology, he even helped me practice a few SDS gels before leaving the lab. Dana was an incredibly supportive mentor and teacher. The students at the University of Central Missouri are lucky to have her.

During my rotations, I was lucky to have amazing mentors too. Thank you to Dr. Ning Zheng and Dr. Rachel Klevit for letting me rotate in your labs. Both labs taught me so much about protein purification and characterization. At these labs, I was lucky to be supervised by Dr. Domnita Rusnac (Zheng) and Dr. Hannah Baughman (Klevit). During my rotation in the King lab, I was mentored by Dr. Karla-Luise Herpoldt who watched me light my hair on fire and still encouraged me to join the lab. I had no biochemistry experience and they all were helpful, kind, and encouraging. I went through an incredibly difficult personal time during my rotation with Domnita and she helped me stay in grad school and became a lifelong friend. Having three amazing women mentor me my first year was something I am truly grateful for.

The people in the King Lab and IPD have truly become like a family to me. Annie, Cara, Grace, Naveen, Mark, Jung Ho, Marti, Erin, Cyrus, Elias, Jeremy, Audrey, Karla, Cassie, Natalie, Gilad, JoJo, and everyone else I had a chance to interact with. Cameron Criswell deserves a special thank you because she worked on TLRs as well. We went through a lot of hard times together and I’m thankful we had each other.

I was incredibly lucky to work with Abby Burtner during her last two years of undergraduate study. She is incredibly talented and an unstoppable force. She is curious and driven. Abby has received more fellowships than I thought humanly possible and she will be one to watch as she continues to pursue her scientific interests.

I am thankful to my Biochemistry cohort and Erin Kirschner who organized us all. My cohort included Kaitlyn Rutter, Andrew Muenks, Erin Yang, Meerit Said, Dane Zambrano, Yuxin Pan, Sidney Lisanza, Madison Kennedy, and others. We survived teaching virtually during the pandemic, a state shutdown, and more.

Ho Min Kim, Hyojin Kim, and Dong Sun Lee were crucial to the structural studies described in Chapter 2. It seemed like we would never obtain structural data and Hyojin worked incredibly hard to obtain unique and difficult to obtain Cryo-EM data.

I am lucky to have a great support network of friends at home who have supported me. Thank you to my virtual book club: Blair Gulick, Anna Thomsen, Mallory Wilhite, Emily Petersen, Tori Tummons, and Jordan Rumsey. Thank you to my Seattle friends and my improv comedy community.

I would like to thank my family for encouraging me and never questioning my cross-country move for grad school. My parents, Samantha McCall and Mark Adams, have always encouraged me to fearlessly pursue my education. They both have visited me, answered my phone calls, and made me feel loved from afar. I am also thankful to my sisters.

Finally, I would like to thank my partner, Neil Gerstenmaier, and our pets, Theo and Loki. Neil always encouraged me and listened to me. He deserves an honorary degree after all of this. He reminded me that I was capable over and over again. And he helped guide me to the light at the end of the tunnel.

Chapter 1. Introduction

Vaccines are a critical part of public health. Historically, vaccines were derived from weakened or inactivated pathogens[1]. Yet, there are limitations to this approach: not all pathogens can be successfully cultured or attenuated[2], and there is concern that weakened pathogens can revert to a replicating pathogen[3]. This has prompted a shift towards subunit vaccines, which use discrete portions of pathogens, making them safer. However, these purified subunits often fail to elicit the robust immune response achieved by whole pathogens. To bridge this gap, adjuvants are incorporated into vaccines to bolster and prolong the immune response.

Adjuvants serve as immunostimulants, enhancing overall immune responses and modulating their nature while conserving antigen doses. Despite substantial advancements in vaccine development over the past three decades, progress in adjuvant research has been slower. Aluminum salts, discovered in the 1920s, reign as the most widely used adjuvant and the field's gold standard[4]. While highly effective and deemed safe, the mechanism of aluminum salts remains incompletely understood, primarily thought to involve a depot effect and inflammasome activation[5]. Additionally, aluminum salts induce a biased Th2 response, which may not be optimal for all pathogens.

Ultimately, the unclear mechanism and biased immune response of aluminum salts have been major shortcomings of this approach. By adsorbing specific immune stimulating molecules onto alum, these issues are somewhat addressed. There is still the issue of formulating and characterizing aluminum with a protein antigen. Characterization methods must be fine tuned to account for the heterogeneity in materials. Additionally, aluminum salts cannot be frozen- making distribution of materials more difficult. We think many of these issues could be alleviated by creating an adjuvant that is protein based. An ideal protein based adjuvant would be stable, specific, and easy to formulate with the antigen.

To create protein based adjuvants, we targeted multiple receptors through a variety of computational methods. Our efforts had different degrees of success but all serve as a launching pad for future efforts. As computational tools continue to make protein design more feasible, it will be important to critically consider receptor biology and vaccine study formulation. Four chapters are outline here describing different receptors we targeted: TLR3, TLR5, TREM-2, and FcγRIIA.

Chapter 2. De novo design of protein minibinder agonists of TLR3

Adapted from: De novo design of protein minibinder agonists of TLR3
https://www.biorxiv.org/content/10.1101/2024.04.17.589973v1

Abstract

Toll-like Receptor 3 (TLR3) is a pattern recognition receptor that initiates antiviral immune responses upon binding double-stranded RNA (dsRNA). Several nucleic acid-based TLR3 agonists have been explored clinically as vaccine adjuvants in cancer and infectious disease, but present substantial manufacturing and formulation challenges. Here, we use computational protein design to create novel miniproteins that bind to human TLR3 with nanomolar affinities. Cryo-EM structures of two minibinders in complex with TLR3 reveal that they bind the target as designed, although one partially unfolds due to steric competition with a nearby N-linked glycan. Multimeric forms of both minibinders induce NF-κB signaling in TLR3-expressing cell lines, demonstrating that they may have therapeutically relevant biological activity. Our work provides a foundation for the development of specific, stable, and easy-to-formulate protein-based agonists of TLRs and other pattern recognition receptors.

Introduction

Toll-like Receptors (TLRs) are a key family of pattern recognition receptors that act as sentinels of the innate immune system. There are 10 TLRs in humans, each of which recognizes a different pathogen-associated molecular pattern: conserved structural or chemical motifs that distinguish microbial pathogens from self[6]. Structurally, the TLRs are type I transmembrane proteins consisting of an extracellular domain, a single transmembrane helix, and an intracellular Toll/IL-1 receptor (TIR) domain[7,8]. The extracellular domain is responsible for ligand recognition and contains multiple leucine-rich repeats (LRRs) that form a horseshoe-like structure[8–11]. Ligand binding drives TLR dimerization and, in some cases, further association into multimeric complexes[12–17]. Multimerization causes the TIR domain to recruit adaptor molecules that activate downstream signaling pathways such as nuclear factor-kappa B (NF-κB) and interferon regulatory factor (IRF) 3 and 7[18,19]. Activation of these signaling pathways leads to the production of pro-inflammatory cytokines, chemokines, and Type I interferons[20–22]. The precise nature of the innate immune response profoundly influences subsequent adaptive immunity[23,24], making targeted modulation of innate immune pathways a promising opportunity to improve the performance of vaccines.

The key role of TLRs in activating the innate immune system makes them ideal targets for vaccine adjuvants: immunostimulators added to vaccines to improve the magnitude, quality, and duration of the adaptive immune response[25,26]. Although aluminum salts are historically the most commonly used adjuvant, over the last quarter century several newer adjuvants with superior performance have been developed that, in some cases, focus on stimulating defined innate immune pathways[27]. For example, a detoxified derivative of the TLR4 agonist lipopolysaccharide (LPS), monophosphoryl lipid A (MPLA), has been formulated with liposomes or aluminum salts in several licensed vaccines[28,29]. The TLR9 agonist CpG has also been licensed as a vaccine adjuvant[30]. Despite this progress, adjuvants are often a bottleneck in vaccine development programs due to intellectual property and safety considerations or formulation difficulties[31,32].

Among the TLRs, TLR3 has several unique features that make it an intriguing target for novel adjuvants. TLR3 is expressed in the endosome in a variety of cells, including myeloid dendritic cells, macrophages, NK cells, and epithelial cells[33,34,35,36]. It is a strong inducer of Type I interferon and is the only TLR that is MyD88-independent, initiating downstream signaling through the TRIF adaptor protein[37,38]. Additionally, TLR3 plays an important role in cross-priming[39,40]. Upon ligand binding, TLR3 forms highly organized and cooperative complexes of dimers that cooperatively assemble along linear dsRNA[16]. However, dsRNA is not an ideal adjuvant due to its instability, structural heterogeneity, and promiscuity[21,41]. Stabilized formulations exist (e.g., poly-ICLC) but are still heterogeneous and activate other immune receptors (MDA-5, RIG-1)[42–45]. This promiscuity can lead to overstimulation and autoimmunity[46]. A chemically well-defined, stable, easy-to-formulate TLR3-specific agonist could alleviate these issues and enable precise, specific induction of TLR3 signaling.

Advances in computational protein design over the last decade have made possible the design of small, hyperstable proteins that can bind specifically to target proteins (“minibinders”)[47–49]. In several cases, minibinders or mimetics of naturally occurring proteins (e.g., cytokines) were shown to be capable of agonizing target receptors and inducing functional biological responses[47,50]. These developments motivate the design of *de novo* TLR agonists, which could potentially form a novel class of protein-based adjuvants. However, TLRs are notoriously difficult targets: they are highly glycosylated, in many cases have no known protein ligands, and are difficult to express and characterize recombinantly[51,52].

Here, we used computational design to generate *de novo* protein minibinders of TLR3. We found that multimeric versions of these minibinders cluster the receptor to initiate signaling, suggesting a route to the *de novo* design of protein-based adjuvants with tailored structural and functional properties.

Results

Computational design of TLR3 minibinders

Although computational methods for designing *de novo* minibinders are now well-established[47], TLR3 is a challenging target for several reasons. First, TLR3, like other TLRs, is highly glycosylated, particularly on the surfaces of the molecule not involved in dsRNA-mediated dimerization[10]. Second, the carbohydrate-free surface of the molecule features many polar residues with few solvent-exposed hydrophobic patches. The combination of these two features made target site selection difficult, as existing minibinder design methods are most successful when targeting hydrophobic surface patches[47]. Third, since our goal was to design minibinder agonists that can drive TLR3 signaling by multimerizing the receptor, we required a target site that would allow oligomeric versions of the minibinder to simultaneously engage multiple TLR3 ectodomains. Taking these three criteria into account, we selected two target sites on human TLR3 (hTLR3; PDB ID: 1ZIW; ref.[11]): Site A, located on the concave face at LRR 19-22 and featuring residues Ile510, Ile534, Ile566, and Ile590; and Site B, spanning LRR 9-11 on the convex face and including residues Leu243, Leu269, Trp273, and Trp296 (**Fig. 1a**). Although both sites are near N-linked glycans, they nevertheless appeared amenable to minibinder design.

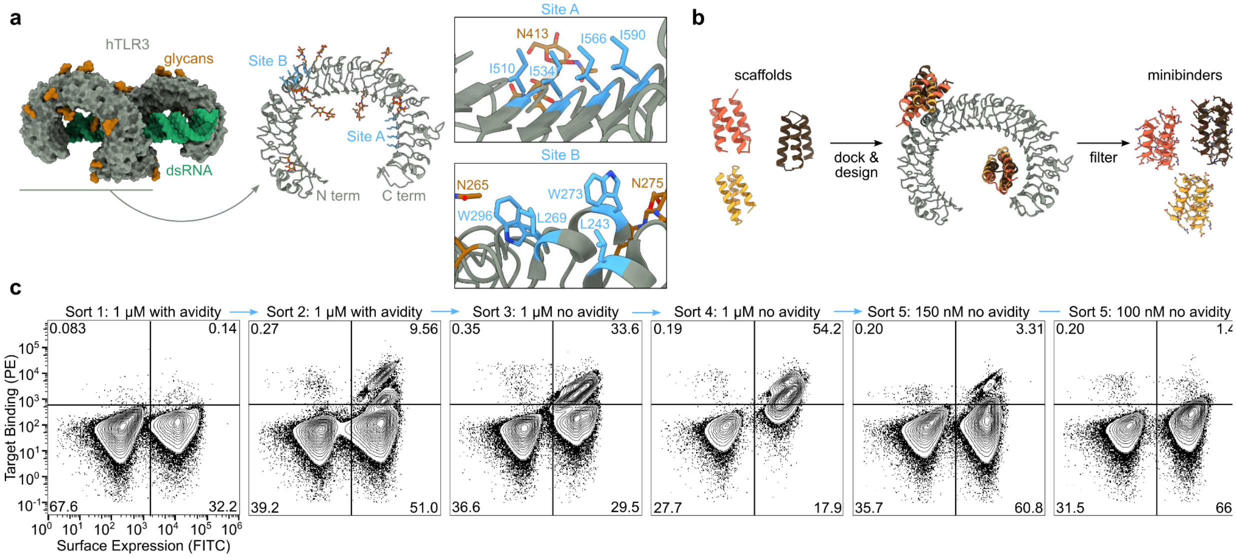

Fig. 1: Computational design of TLR3 minibinders.

a, *Left,* TLR3 is natively dimerized and activated by dsRNA (PDB ID: 7WV5). *Right*, two hydrophobic patches on the TLR3 monomer were targeted for minibinder design (PDB ID: 1ZIW). **b,** Polyvaline scaffolds were used in the RifDock pipeline to design *de novo* miniprotein binders. Several structural metrics were used as filters to select 23,789 designs for experimental screening. **c,** Binders were identified using yeast surface display. During Sort 5, binding was clearly observed at 150 nM receptor, but approached levels of background signal at 100 nM.

We used the Rosetta RifDock pipeline[47] to design a library of candidate TLR3 minibinders (**Fig. 1b**). We first used RifGen[53] to dock disembodied amino acid side chains against Sites A and B, and in parallel docked 21,402 pre-existing polyvaline scaffolds (i.e., backbones) against the same sites using PatchDock[48,53]. Docks that matched the most high-scoring disembodied sidechains were output from RifDock and passed to Rosetta FastDesign[48] to generate designed amino acid sequences. The designs were evaluated for predicted binding energy (ddG), contact molecular surface to hydrophobic residues, and spatial aggregation propensity (SAP)[54], and the best-scoring interfaces were extracted using MotifGraft and subjected to a second round of FastDesign. After filtering using the computational metrics described above, we selected 23,789 designs for experimental characterization: 52% targeting Site B and 48% targeting Site A.

We cloned synthetic oligonucleotides encoding the designs into an expression vector to enable screening by yeast surface display[55] and used fluorescence-activated cell sorting (FACS) to identify cells expressing miniproteins that bound fluorescently labeled TLR3 ectodomain. After two rounds of sorting with 1 μM streptavidin-tetramerized TLR3 as a probe, we observed a clear population of double-positive cells (**Fig. 1c**). Enrichment of this population by subsequent sorts without avidity (i.e., with monomeric TLR3) resulted in high numbers of TLR3-binding cells at 150 nM receptor that decreased to near-background levels at 100 nM. Sequencing double-positive cells from each sort identified 11 hits out of 23,789 candidates, a success rate consistent with previous applications of this methodology[47].

Biochemical characterization of TLR3 minibinders

All 11 of the hits identified by FACS target Site A. We suspect that the proximity of Site B to the aforementioned N-linked glycans likely prevented binding at this site. The computational design models of the hits show that they adopt a variety of binding modes within Site A (**Fig. 2a, Extended Data Fig. 1**). We expressed each with a

C-terminal Avi-His$_6$ tag in *E. coli* and purified them by immobilized metal affinity chromatography (IMAC) and size exclusion chromatography (SEC) (**Fig. 2b, Extended Data Fig. 1**). To validate target binding, the minibinders were biotinylated and their affinities to hTLR3 were determined using Bio-Layer Interferometry (BLI). Six of the eleven minibinders bound to hTLR3 with affinities ranging from 43–1,500 nM; minibinders 6, 7, and 8 yielded the highest binding amplitudes (**Fig. 2c, Extended Data Fig. 1**).

To evaluate the binding mode of each minibinder and identify mutations that enhance affinity to TLR3, we created a Site-Saturation Mutagenesis (SSM) library for each minibinder by systematically mutating each residue to all 19 other canonical amino acids. We sorted a single, pooled SSM library comprising 11,823 variants based on all 11 original minibinders using FACS and detected binding down to 125 nM, similar to the original library (**Extended Data Fig. 2a**). Deep sequencing of the sorted libraries allowed us to visualize the effect of each mutation using heatmaps, where red signifies stronger binding and blue indicates weaker binding (**Fig. 2d, Supplementary File 1**). Minibinders 9 and 10 were deprioritized at this stage due to inconsistencies between their design models and SSM data that suggested these minibinders did not fold as predicted. In other cases the SSM data were consistent with the design models, as indicated by, for example, generally high conservation of amino acids predicted to make substantial interactions with the TLR3. In general, each minibinder had one helix which did not make contact with TLR3 and was less conserved. At some positions, substitutions that appeared to enhance binding to TLR3 could be identified. The interface of minibinder 7 appeared more amenable to a wider variety of interface mutations than minibinder 8, such as L16V/I/M/Y/W in minibinder 7 compared to F33Y in minibinder 8. We selected several such mutations for minibinders 1-8 and 11 and integrated them into combinatorial yeast display libraries for each minibinder using degenerate codons (**Supplementary Table 1**). During FACS of a pool of these combinatorial libraries, we observed binding at TLR3 concentrations as low as 50 nM, an improvement over the SSM libraries that suggested that combining mutations improved binding more effectively than single mutations (**Extended Data Fig. 2b**). All of the hits obtained by deep sequencing in the sorted combinatorial library were derived from minibinder 7. We ordered 12 of these variants, named minibinders 7.1–7.12, for expression in *E. coli* (**Supplementary Table 1**). We also noted that of the three minibinders with the strongest initial binding amplitudes during BLI (minibinders 6, 7, and 8), minibinders 6 and 7 had very similar predicted binding modes (**Fig. 2a** and **Extended Data Fig. 1**) and eluted at fractions corresponding to higher molecular weights than expected during SEC (**Fig. 2c, Extended Data Fig. 1**), potentially indicating that they homodimerize. By contrast, minibinder 8 was predicted to bind further from the N413 glycan compared to minibinders 6-7 and eluted from SEC at the expected volume for a monomer (**Fig. 2a,b**). We therefore chose to also optimize minibinder 8 in addition to minibinder 7, and ordered six variants comprising one or more mutations manually selected from the SSM data for expression in *E. coli* (**Supplementary Table 1**).

We expressed and purified the affinity-matured variants of minibinders 7 and 8 (**Extended Data Figs. 3, 4**) and found that each bound hTLR3 with a tighter K_D than the parent minibinder. For minibinder 7 variants, K_D ranged from 1.1–190 nM, whereas for minibinder 8 variants, K_D ranged from 37–690 nM (**Fig. 2e; Extended Data Figs. 3, 4**). To obtain initial structural information, we performed circular dichroism (CD) on minibinders 7.1 and 8.6 (K_D = 48 and 37 nM, respectively). At 25°C both minibinders yielded spectra typical of α-helical proteins, although the amplitude of the signal was stronger for minibinder 8.6 (**Fig. 2f**). Heating the proteins to 95°C and then returning them to 25°C showed that both unfolded at high temperature and regained their native structure upon cooling.

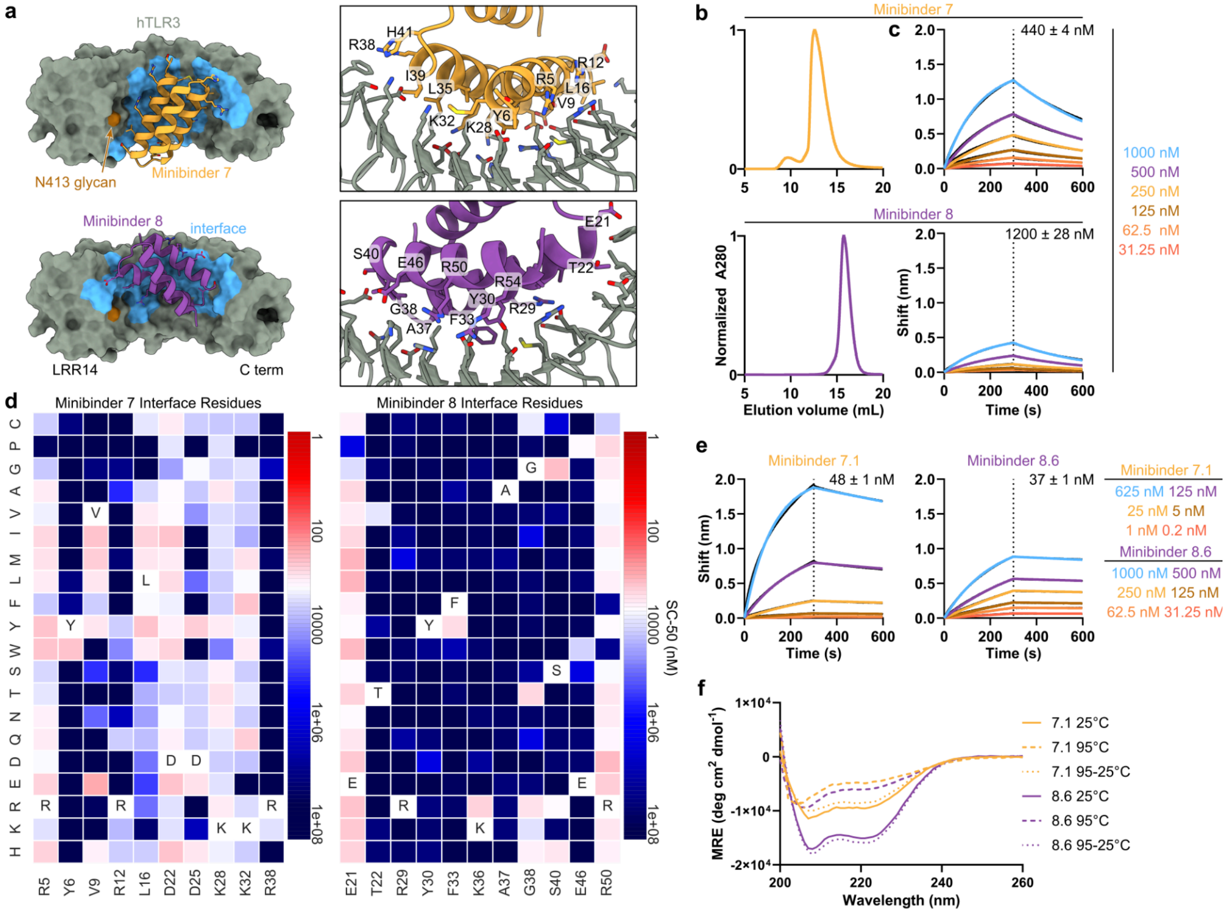

Fig. 2: Biochemical characterization and affinity maturation of lead TLR3 minibinders.

a, Design models of minibinders 7 (yellow) and 8 (purple) in complex with TLR3 (gray). The details of the predicted interface are shown at right. **b,** Size exclusion chromatograms of each minibinder on a Superdex 75 10/300 GL. **c,** Affinity determination for each minibinder by BLI. The concentrations of hTLR3 used are listed. The black lines represent experimental data and the colored lines represent fits. K_D values are given. **d,** Site saturation mutagenesis heat maps of interface residues. The originally designed amino acid at each position is provided at the bottom and in the white square. Red indicates affinity improvement and blue indicates affinity reduction. **e,** Biolayer interferometry of affinity-matured minibinders 7.1 and 8.6. K_D values are given. **f,** CD of affinity-matured constructs at various temperatures. Solid line, 25°C; dashed line, 95°C; dotted line, 95°C followed by 25°C.

Structural characterization of minibinder-TLR3 complexes

We selected minibinders 7.7 and 8.6 for structural studies, as these variants exhibited high association rates and low dissociation rates by BLI (**Fig. 2e, Supplementary Table 2**). We began by mixing minibinder 7.7 with purified human TLR3 (residues K27-A700) *in vitro* and imaging vitrified specimens by cryo-electron microscopy (cryo-EM). Although a minority of the 2D class averages had density potentially corresponding to the minibinder at target Site A, overall the data suggested low minibinder occupancy. We therefore co-expressed the TLR3 ectodomain and each minibinder in HEK293F cells and co-purified the complexes using affinity chromatography followed by SEC. After optimizing grid preparation and data collection to overcome a clear preferred orientation, we determined cryo-EM structures of minibinders 7.7 and 8.6 in complex with TLR3, each at 2.9 Å resolution (**Fig. 3, Extended Data Figs. 5** and **6**). This resolution permitted us to manually build atomic models of TLR3 and the minibinders into the cryo-EM maps. In both structures, TLR3 closely resembled previously reported structures, exhibiting Cα root mean square deviations (RMSDs) of 1.78 Å for 7WV3 and 1.61 Å for 7C76 (refs.[16,56]). Unlike minibinder 8.6, for which clear density was observed for all three α-helices, we could build only α1 and α2 of minibinder 7.7 into well-defined density (**Fig. 3a**). Interestingly, density corresponding to α3 of minibinder 7.7 could be observed extending from α2 at a low threshold (0.08 σ; **Extended Data Fig. 7a**). Given the proximity of the minibinder to the glycan at N413, we conclude that a steric clash between the glycan and minibinder 7.7 makes α3 protrude out from the complex. This conclusion is supported by our SSM data for minibinder 7—obtained in complex with TLR3—which showed that mutations in the hydrophobic core were more tolerated than would be expected for a well-folded protein (**Supplementary File 1**). Although it is difficult to discern whether α3 is well-packed against α1 and α2 in the absence of TLR3, we note that CD of the closely related minibinder 7.1 suggested it is less α-helical than minibinder 8.6 (**Fig. 2f**).

Minibinders 7.7 and 8.6 interacted with the concave surface of TLR3 in slightly different manners, with α1 and α2 of minibinder 7.7 binding to LRR15-LRRCT and α2 and α3 of minibinder 8.6 binding to LRR13-LRRCT. Hydrophobic residues on both minibinders (7.7: M3, Y6, L35, V36, and I39; 8.6: Y30, Y33, A34, V43, L47, and V51) form hydrophobic networks with I510, I534, I566, and I590 in Site A of TLR3 as intended (**Fig. 3a, 3c and 3f, Extended Data Figs. 7b and 7c**). When the cryo-EM structures were superimposed on the AlphaFold2-predicted models of each complex, the Cα RMSDs between minibinders 7.7 and 8.6 and their predictions were 1.0 and 2.0 Å, respectively (**Fig. 3b**). For minibinder 8.6, the α2 and α3 helices were well-aligned (Cα RMSD: 1.6 Å), but α1 was slightly displaced from its predicted position (Cα RMSD: 2.7 Å). The altered conformation of minibinder 7.7 α3 described above may result in exposure of hydrophobic residues in the protein core to solvent (e.g., L11 and L30). Alternatively, they may interact with the N413 glycan, although we did not observe ordered density in this region of the map (**Extended Data Fig. 7a and 7b**). Conversely, minibinder 8.6 maintained a stable 3-helical bundle through core hydrophobic interactions (**Extended Data Fig. 7c**).

The interactions between minibinder 7.7 and TLR3 were mainly mediated through electrostatic interactions (**Fig. 3c-e and Extended Data Figs. 8 and 9**). Specifically, our structural analysis revealed that conserved residues (Y6, R12, E19, and D22) in minibinder 7 and its derivatives engaged in hydrogen bonds or ionic interactions with residues on the concave surface of TLR3. Residues E9, Y25, K28, and K32 of minibinder 7.7 were crucial for forming electrostatic interactions with TLR3 (**Fig. 3c-3e and Extended Data Fig. 8 and 9**). In contrast to minibinder 7.7, the electrostatic interactions mediated by Y33 and conserved residues (R29, Y30, K/R36, E42, E46) in minibinder 8 and its derivatives surround a hydrophobic core interaction network in the minibinder 8.6/TLR3 complex (**Fig. 3f and 3h, and Extended Data Fig. 8 and 9**). Interestingly, our structural analysis revealed that the interaction of T38 with A35 and I44 stabilizes the loop connecting α2 and α3, facilitating the formation of hydrogen bonds between S40 and E42 of minibinder 8.6 and E639 and N667 of TLR3, respectively (**Fig. 3g and Extended Data Fig. 8 and 9**). Additionally, the R50D substitution in minibinder 8.6 enabled the formation of an ionic interaction with K589 of TLR3. These observations likely explain why the G38T and R50D substitutions significantly enhanced the binding affinity of minibinder 8.6 compared to 8.4.

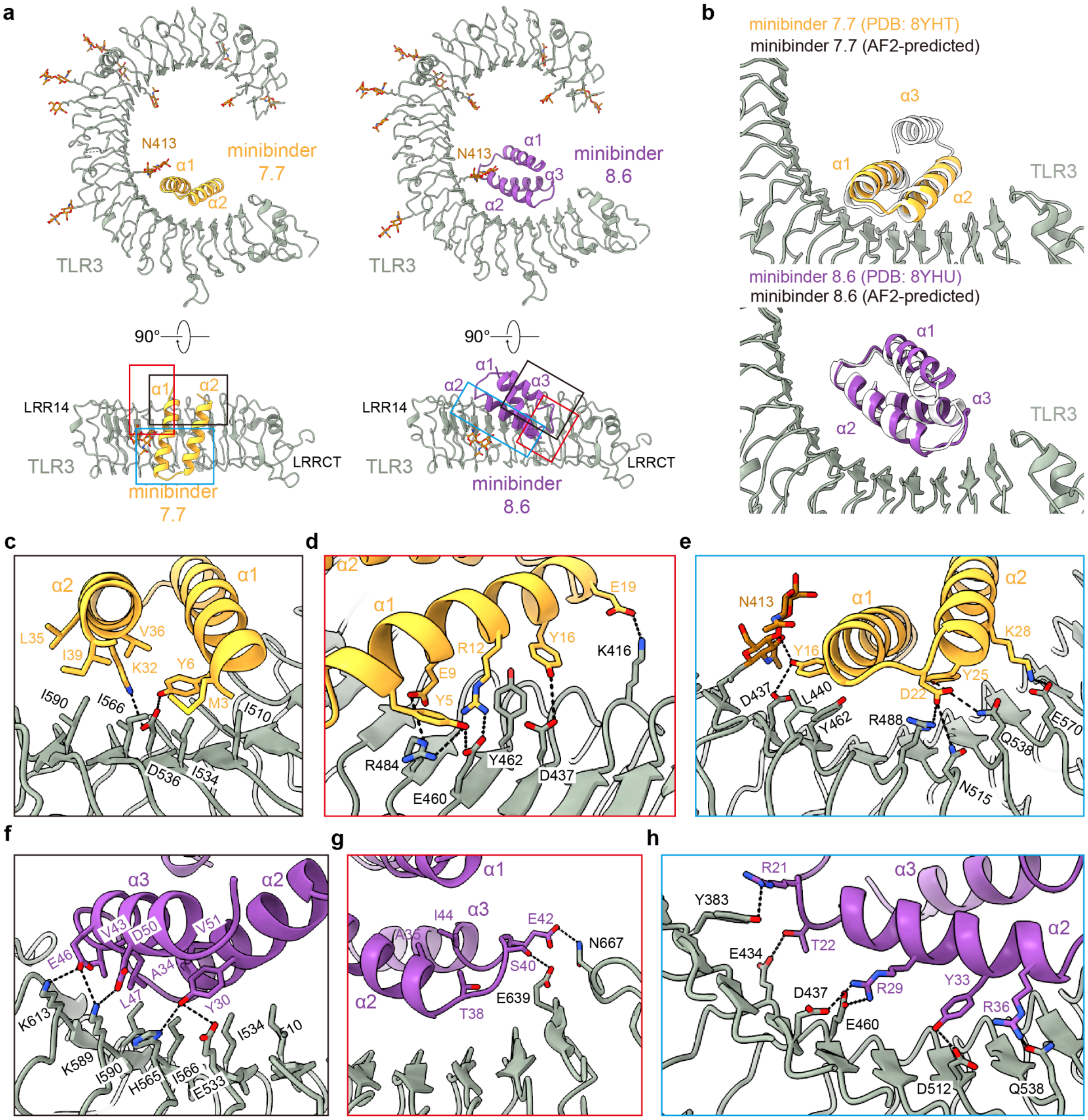

Fig. 3: Structural characterization of TLR3 minibinders.

a, Two different views of the cryo-EM structures of human TLR3 in complex with minibinder 7.7 (left) or minibinder 8.6 (right). TLR3, glycans, minibinder 7.7, and minibinder 8.6 are in gray, brown, yellow, and purple, respectively. **b,** Comparison of experimental and AlphaFold2-predicted structures of the minibinders in complex with TLR3. **c-h,** Close-up views of key molecular interactions in TLR3/minibinder 7.7 (**c-e**) or TLR3/minibinder 8.6 (**f-h**). Each box is a close-up view of the same colored box in **a**. Residues involved in the TLR3/minibinder interaction are displayed as sticks and labeled.

Activation of TLR3 by multimerized minibinders

Like other TLRs, the minimal signaling unit of TLR3 is a ligand-induced dimer[57], although maximal TLR3 signaling requires lateral association of TLR3 dimers, an arrangement facilitated by the linear nature of dsRNA[12,16,17]. We next investigated whether we could engineer our minibinders to drive TLR3 multimerization and thus activation. We approached this problem by generating two different multimeric forms of our affinity-matured minibinders. In the first, we genetically fused four copies of either minibinder 7.1 or 8.6 in tandem using 16-residue flexible linkers to create minibinder tetramers that could associate with two or potentially more copies of TLR3 (**Fig. 4a**). In the second, we genetically fused minibinder 8.6 to the C terminus of an antiparallel coiled-coil derived from myosin 10 (PDB ID: 2N9B)[58] to generate minibinder dimers that roughly match the geometry of the dsRNA-induced TLR3 dimer (**Fig. 4b**). We expressed and purified the 7.1 tetramer, the 8.6 dimer, and the 8.6 tetramer and confirmed that they bind to TLR3 by BLI (**Extended Data Fig. 10a,b**). As negative controls, we also purified "interface knockout" versions of each protein that incorporate mutations shown to decrease TLR3 binding in our earlier SSM data (**Supplementary Table 1**). We determined by BLI that the interface knockout mutations nearly eliminated TLR3 binding in monomeric and multimeric versions of minibinders 7 and 8 (**Extended Data Fig. 10b,c**).

To assess TLR3 activation, we used TLR3hi cells, a previously described HEK293 cell line that expresses TLR3 on the cell surface and features an NF-κB-linked GFP reporter[57] (**Fig. 4c**). We first confirmed that known TLR3 agonists activated the cells by flow cytometry. Cells stimulated with poly(I:C) at concentrations ranging from 0.3–20 μg/mL robustly expressed GFP, and modest GFP expression was still detectable at 0.02 μg/mL (**Fig. 4d,e**). Polyclonal anti-TLR3 antibody also induced GFP expression as previously shown[57], while a control goat polyclonal antibody did not. Finally, lipopolysaccharide (LPS) failed to induce GFP expression, demonstrating that TLR4 signaling was inactive in the cells.

We stimulated the cells with each of our minibinder multimers and their corresponding interface knockouts at 300, 100, and 33 μg/mL, as well as the minibinder monomers at 300 μg/mL. We found that the 7.1 tetramer and the 8.6 dimer induced comparable levels of dose-dependent GFP expression (**Fig. 4d,e**). The 7 knockout (KO) tetramer yielded substantially reduced but still dose-dependent GFP expression, while GFP expression in cells treated with the 8 KO dimer was not above background. In each case, activation with monomeric minibinder was substantially lower than with the same concentration of multimer. The 8.6 tetramer activated TLR3 more efficiently; GFP expression was higher in cells treated with 33 μg/mL of the 8.6 tetramer than in cells receiving 9-fold more 8.6 dimer or 7.1 tetramer. At the highest concentration tested, the 8.6 tetramer induced GFP expression as effectively as moderate concentrations of poly(I:C). These data establish that our TLR3 minibinders become agonists when multimerized, presumably by clustering multiple copies of TLR3 in close proximity.

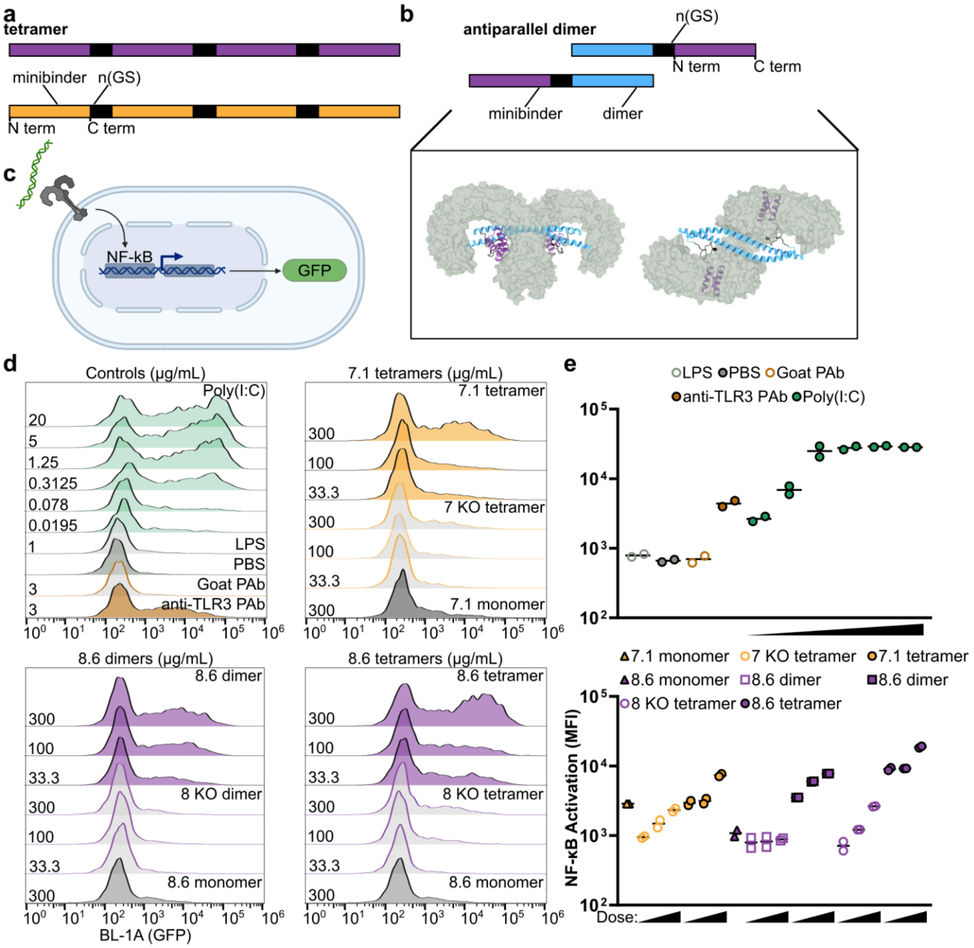

Fig. 4: Multimerization of minibinders leads to NF-κB activation.

a, Minibinder tetramers were generated by fusing four tandem repeats of the minibinder together using 16-residue (GlySer) linkers. **b,** Antiparallel 8.6 dimers were generated by fusing minibinder 8.6 to the C terminus of an antiparallel coiled-coil derived from myosin 10. Two views of a model of the 8.6 dimer in complex with hTLR3 are shown. **c,** TLR3 is expressed on the cell surface of TLR3hi cells, which express an NF-κB-linked GFP reporter. **d,** Histograms showing GFP signal in stimulated TLR3hi cells. The identities and concentrations of the stimuli are provided on the right and left sides of each panel, respectively. **e,** Mean fluorescence intensity (MFI) values from assay duplicates. Concentrations are provided in **d**.

Discussion

Our results demonstrate that computational protein design can be used to create stable protein agonists of TLR3. Historically, TLR agonist discovery has focused on making stabilized or safer forms of native ligands (e.g., poly(I:C), MPLA, CBLB502) or making small-molecule mimics of them (e.g., R848, 3M-052)[59–63]. The approach described here could have several advantages when considering the use of minibinder agonists as "protein-based adjuvants." First, many vaccine antigens are proteins, which may enable the seamless integration of antigen and minibinder adjuvant into a single molecule by genetic fusion[64–68]. This strategy would be expected to simplify manufacturing and formulation compared to traditional nucleic acid, lipid, or small molecule adjuvants. Second, the genetic basis of protein-based adjuvants enables them to be encoded in DNA or mRNA vaccines[69,70], which is impossible for non-biological compounds such as alum or 3M-052. Although cytokines have been explored extensively as genetically encoded adjuvants, to date it has not been possible to target TLRs in this way other than TLR5, which has a protein as its native ligand (flagellin)[71–73]. Finally, many native TLR ligands such as dsRNA, flagellin, and LPS initiate signaling through multiple distinct receptors[74–78]. Designing miniprotein agonists that specifically activate individual innate immune receptors, or desired combinations thereof, should in principle allow precise tuning of vaccine-elicited immune responses[79]. Further work will be required to explore the advantages and disadvantages of this strategy.

There are multiple structures of TLR3 in complex with Fabs or diabodies, all of which target epitopes on the convex surface of the receptor[16,17,80]. Here, minibinders 7 and 8 and their derivatives bind to the concave surface of TLR3. This proved to be a challenging target due to the polar and highly glycosylated surface of the molecule. Due to a nearby glycan, the third helix of minibinder 7.7 was disordered when bound to TLR3, a phenomenon that has not been documented before in designed minibinders to the best of our knowledge. Although this possibly accounts for the weaker agonism of 7.1 tetramers compared to 8.6 tetramers, it is an intriguing observation that suggests steric competition with glycans or other parts of a target protein structure could be used as a mechanism for intentionally introducing switching behavior in designed minibinders[81].

When multimerized, our minibinders activated NF-κB via TLR3 in a cell line that expresses TLR3 on the cell surface. Additional studies will be required to develop protein-based TLR3 agonists that function as vaccine adjuvants *in vivo*, where they must reach the endosome of cells expressing the receptor. Furthermore, previous studies showed that the minimal TLR3 signaling complex in the TLR3hi cell line is a dimer[57]. However, several additional reports, including recent cryo-EM structures of TLR3 in complex with dsRNA, have shown that the formation of linear polymers of TLR3 dimers along longer dsRNA molecules is required for maximal activation[12,16,17]. It is likely that the activity of our minibinder agonists could be improved by multimerizing them so that they match the geometry of the fully active signaling complex. Supporting this notion, a recent study of designed multimeric cytokines established that tuning the precise geometry of receptor clustering through design can significantly impact activation and signaling[82]. Combining our approach to TLR minibinder design with recently developed generative methods for designing multimeric scaffolds[83] could become a powerful and general approach to designing protein-based TLR agonists.

Acknowledgements

The findings in this chapter are reported in a BioRxiv preprint (https://www.biorxiv.org/content/10.1101/2024.04.17.589973v1). The authors are Chloe S. Adams, Hyojin Kim, Abigail E. Burtner, Dong Sun Lee, Craig Dobbins, Cameron Criswell, Brian Coventry, Ho Min Kim, and Neil P. King. H.M.K. and N.P.K. are co-corresponding authors. C.S.A. and B.C. designed minibinders. C.S.A. and C.C. performed computational analysis of designs. C.S.A. and A.E.B. screened designs and carried out biochemical characterization. C.S.A. and C.D. performed cell-based assays. H.K., D.S.L., and H.M.K. designed and carried out electron microscopy experiments. N.P.K. and H.M.K. supervised research. C.S.A., H.K., H.M.K., and N.P.K. wrote the paper. We would like to thank Andrew Borst, Jung Ho Chun, Xinru Wang, Joseph Harman, Jing Yang Wang, Naveen Jasti, Naveen Mehta, Daniel Humphrys, Madison Kennedy and Sidney Lisanza for helpful discussions; Joshua Leonard and Amparo Cosio for generously providing TLR3hi cells; and Inna Goreshnik, Aza Allen, Cami Cordray, Samer Halabiya, and Dionne Vafeados for help with yeast library preparation. We are grateful to the staff of the Research Solution Center at IBS for help with cryo-EM data collection. Cryo-EM data processing was performed on Olaf, the data analysis hub in the IBS Research Solution Center. This work was supported by grants from the Bill & Melinda Gates Foundation (INV-010680 and INV-043758 to N.P.K.), the Institute for Basic Science (IBS-R030-C1 to H.K. and H.M.K.), the NIH (T32GM008268 to C.S.A.). A.B. was supported by a Washington Research Foundation Fellowship, the Barry Goldwater Scholarship, and the Audacious Project at the Institute for Protein Design.

Materials and Methods

Computational design

The ectodomain of TLR3 (PDB ID: 1ZIW) was used for the design. The PDB was truncated to save computational time. Minibinders were designed as outlined in ref.[47]. In brief, RifGen[53], PatchDock[84], RifDock[53], FastDesign[48], and the MotifGraft mover[85] were used. Millions of designs were created using this pipeline and then filtered on various Rosetta metrics (contact molecular surface to hydrophobic residues, ddG, and SAP)[47]. Designs before and after the MotifGraft stage were ordered.

Library preparation

Designs were padded to 65 amino acids with serine. Then, the designs were codon-optimized for expression in *Saccharomyces cerevisiae*. Oligonucleotides encoding the designs and SSM mutations were purchased from Agilent technologies. Libraries were amplified as previously described[47].

Yeast surface display

Minibinders were displayed on the surface of yeast with a C-terminal myc tag to enable detection of cell surface expression using a FITC-labeled anti-myc antibody. Biotinylated hTLR3 ectodomain was recognized by streptavidin-PE. An initial sort was done to collect cells that express the designs (FITC+). These cells were subsequently sorted against decreasing concentrations of hTLR3 with and without avidity.

The *Saccharomyces cerevisiae* EBY100 strain was cultured in C-Trp-Ura medium containing 2% (w/v) glucose (CTUG). For induction, cells were harvested by centrifugation at 5,000 g for 5 minutes and subsequently resuspended in SGCAA medium supplemented with 0.2% (w/v) glucose at a cell density of 1×10^7 cells per mL. The cells grew at a temperature of 30°C for 16-24 hours. After induction, the cells were washed using PBSF (PBS with 1% (w/v) BSA). The cells were labeled with anti-c-Myc fluorescein isothiocyanate (FITC, Miltenyi Biotech) and streptavidin-phycoerythrin (SAPE, ThermoFisher).

During the initial sorting of the naive library, an avidity-based approach was employed. This entailed simultaneous incubation of the biotinylated target, SAPE, and FITC. In contrast, sorts performed without avidity involved a sequential procedure. Specifically, cells were incubated with the biotinylated target, washed with PBSF, and then incubated with SAPE and FITC.

Deep sequence analysis

Collected sorts were sequenced using Illumina NextSeq sequencing and analyzed using the PEAR program[86] as previously described[47].

Protein expression and purification

Genes encoding minibinders were synthesized and cloned by Integrated DNA Technologies into a pET-29b(+) vector. Plasmids were transformed into BL21(DE3) (NEB) and 30 mL of single-colony culture was grown in Terrific Broth II (MP Biomedical) at 37°C overnight. 25 mL was transferred to 0.5L of autoinduction medium and grown at 37°C for 2 hr and 18°C overnight[87]. Cells were collected by spinning for 30 min at 4000 g. Pellets were resuspended in lysis buffer (50 mM Tris pH 8.0, 250 mM NaCl, 20 mM imidazole, 0.04 mg/mL RNase, 0.1 mg/mL lysozyme, 0.1 mg/mL DNase, 1 mM PMSF). The cells were lysed via a microfluidizer. The lysed cells were clarified via centrifugation at 14,000g for 30 min. The supernatant was run over Nickel-NTA resin and washed with 3 CV of wash buffer (50 mM Tris pH 8.0, 250 mM NaCl, 20 mM imidazole). Protein was eluted with an elution buffer (50 mM Tris pH 8.0, 250 mM NaCl, 500 mM imidazole) and further purified by size exclusion chromatography using a Superdex S75 10/300 GL column (Cytiva). The multimers of minibinders were purified using a Superdex S200 5/150 GL column (Cytiva).

The TLR3 ectodomain used for yeast display and BLI was obtained from Wuxi Biologics (custom order). The sequence is derived from Choe *et al.*[11] and included a Gp67 signal peptide and C-terminal His and Avi tags (**Supplementary Table 1**). To produce the protein, a baculovirus was generated using Sf9 cells and High Five cells were used for protein expression. The final buffer was 50 mM Tris, 250 mM NaCl, 1 mM DTT.

Biolayer interferometry

BLI was performed on an Octet RED96 or Octet R8. All biosensors were hydrated in kinetics buffer HBS-EP+ (10 mM HEPES, 150 mM NaCl, 3 mM EDTA, 0.05% v/v surfactant P20) with 0.5% w/v non-fat dry milk (Cytiva). Minibinders were biotinylated and excess biotin was purified out by SEC. Biotinylated minibinders were diluted to a final concentration of 0.01 mg/mL in kinetics buffer and loaded onto streptavidin biosensors (Sartorius). TLR3 was diluted in kinetics buffer and its association was measured for 300 s, followed by a dissociation for 300 s in kinetics buffer.

For the constructs used in the cell assay, Human TLR3-FC (Acro Biosystems) was diluted to 0.01 mg/mL in kinetics buffer and loaded onto Protein A tips (Sartorius). The cell assay constructs were diluted to 10 µM in kinetics buffer and their association was measured for 300 s, followed by a dissociation for 300 s in kinetics buffer.

Combinatorial library preparation

We identified mutations that enhanced affinity from SSM heatmaps. We then used SwiftLib to create libraries containing these mutations with degenerate codons[88]. We ordered 2 overlapping Ultramers for each design that contained these degenerate codons (Integrated DNA Technologies). The ultramers were stitched together and cloned into yeast. All libraries were combined before yeast surface display.

Circular dichroism

CD measurements were carried out on a JASCO J1500 spectrometer at 25°C-95°C, using a 1 mm path-length cuvette, at wavelengths from 200 to 260 nm. Proteins were measured at 0.4 mg/mL in PBS buffer.

Constructs for recombinant expression of TLR3/minibinder complexes

Human TLR3 ectodomain (residues K27-A700) followed by a 6× His-tag was cloned into the BamHI and XbaI sites of the pcDNA 3.1 vector (#V79020, Invitrogen) containing the vascular endothelial growth factor receptor 1 (VEGFR) signal sequence for protein secretion. Residues S1-L56 of minibinder 7.7 or residues S1-S56 of minibinder 8.6 followed by a thrombin cleavage site and Protein A-tag were cloned into the BamHI and EcoRI sites of the pcDNA 3.1 vector containing the VEGFR signal sequence for protein secretion.

Expression and purification of the TLR3/minibinder complex for cryo-EM

A total of 1 μg of plasmid DNA (TLR3:minibinder-protein A ratio of 1:4) was transfected into 2.5×10^6 Expi 293F cells (#A14527, Thermo Fisher Scientific) using Expifectamine (#A14524, Thermo Fisher Scientific), and cells were cultured in Expi293 expression medium (#A14351, Thermo Fisher Scientific) at 37°C and 8% CO2 with shaking (orbital shaker, 120 rpm) for 4 days. After centrifugation to remove the cells, the culture supernatant was loaded onto IgG Sepharose 6 Fast Flow (#17-0969-01, Cytiva). After washing with 10 column volumes of wash buffer (20 mM Tris-HCl pH 8.0, 200 mM NaCl), the Protein A–fused binary complexes (TLR3/minibinder-protein A) bound to the resin were incubated with thrombin (1% [v/v] in wash buffer) at 4°C for 16 h to remove the C-terminal Protein A tag. The eluted TLR3/minibinder complexes were concentrated to 1 mg/mL using an Amicon Ultra centrifugal filter (#UFC8030, Millipore) and further purified by SEC using a Superdex 200 Increase 10/300 GL column (#GE28-9909-44, Cytiva) equilibrated in wash buffer (20 mM Tris-HCl pH 8.0, 200 mM NaCl). The peak fraction was used for cryo-EM analyses without concentration.

Cryo-EM sample preparation and data collection

Initially, the use of a general quantifoil grid led to a preferred orientation in the 2D average of the initial dataset, showing only C-shaped side views of the TLR3/minibinder complex. This limitation caused the 3D volume to stretch sideways, preventing the generation of a high-resolution reconstruction. It is known that coating the cryo-EM grid with a clean graphene oxide layer can help the protein particles adopt various orientations[89]. Indeed, graphene oxide-coated grids resulted in 20% of views from other angles, while approximately 80% of the particles still displayed the C-shaped view. Graphene oxide-coated Quantifoil R1.2/1.3 300 mesh copper holey carbon grids (Quantifoil Micro Tools) were glow discharged using a PELCO easiGlow Glow Discharge Cleaning system (Ted Pella) for 5 s at 10 mA. 3 μL of the purified TLR3/minibinder complexes were applied to the grid and incubated for 10s in 100% humidity at 4°C. After 2 s of blotting, the grid was plunged into liquid ethane using a Vitrobot MkIV (Thermo Fisher Scientific). Micrographs were acquired on a Titan Krios G4 TEM operated at 300 keV with a K3 direct electron detector (Gatan) at the Institute for Basic Science (IBS), using a slit width of 20 eV on a GIF-quantum energy filter. EPU software was used for automated data collection at a calibrated magnification of 130,000× under the single-electron counting mode and correlated-double sampling (CDS) mode[90], yielding a pixel size of 0.664 Å/pixel. Detailed image acquisition parameters for each TLR3/minibinder complex are summarized in **Supplementary Table 3**.

Image processing, model building, and refinement

The detailed image processing workflow and statistics are summarized in **Extended Data Figs. 5 and 6** and **Supplementary Table 3**. Raw movies were motion-corrected using MotionCorr2[91], and the CTF parameters were estimated by CTFFIND4[92]. All other image processing was performed using cryoSPARC v.4.2.1[93]. Initially, particles were picked with a manual picker of cryoSPARC from a few micrographs. 2D class averages representing projections in different orientations selected from the initial 2D classification were used as templates for automatic particle picking from whole micrographs. The resulting particles went through subsequent 2D classifications for cleanup within cryoSPARC.

Even though the preferred orientation was slightly improved using the graphene oxide-coated grid, approximately 80% of the particles were still included in the C-shaped views. To find the best ratio between views that can create a nice 3D volume by making the Euler angle distribution as even as possible, we tested various ratios of C-shaped views and other views using Rebalance 2D in cryoSPARC. Robust 3D volumes were generated using twice as many C-shaped particle views as other views by removing ~40% of the C-shaped view from the dataset. Non-uniform refinement[94], local motion correction[95], and CTF refinement[96] improved the particle alignment and map quality. The final refinement yielded a map at an overall ~3.0 Å resolution (with tight mask). The mask-corrected Fourier shell correlation (FSC) curves were calculated in cryoSPARC, and reported resolutions were based on the gold-standard Fourier shell correlation (FSC) = 0.143 criterion[97]. Local resolutions of density maps were estimated by Blocres[98].

Model building for TLR3 was initiated by docking the AlphaFold2-predicted TLR3 into the post-processed cryo-EM map generated from DeepEMhancer[99] using the Phenix package. The Cα chain and side chains of minibinders were manually built in the cryo-EM density map using Coot[100], referring to their AlphaFold2-predicted structure. Models of the TLR3/minibinder complexes were manually adjusted in Coot and refined against the map by using the real space refinement in the Phenix package. The refinement statistics from Phenix validation are summarized in **Supplementary Table 3**.

Cell assay

HEK293-TLR3hi cells were cultured in DMEM with 4 mM L-glutamine (ThermoFisher), 10% FBS (ThermoFisher), 1% penicillin-streptomycin (ThermoFisher), and 500 µg/mL G418 sulfate (ThermoFisher). 10^5 cells were plated in a 24-well plate in 0.25 mL of media for 3 hours. Ligand was added and 24 hours later NF-κB-driven GFP expression was measured using flow cytometry on an Attune NxT. Poly(I:C) HMW (InvivoGen) and polyclonal goat anti-TLR3 (R&D systems) were used as positive controls. LPS-B5 (InvivoGen) and polyclonal goat IgG (R&D systems) were used as negative controls.

Extended Data

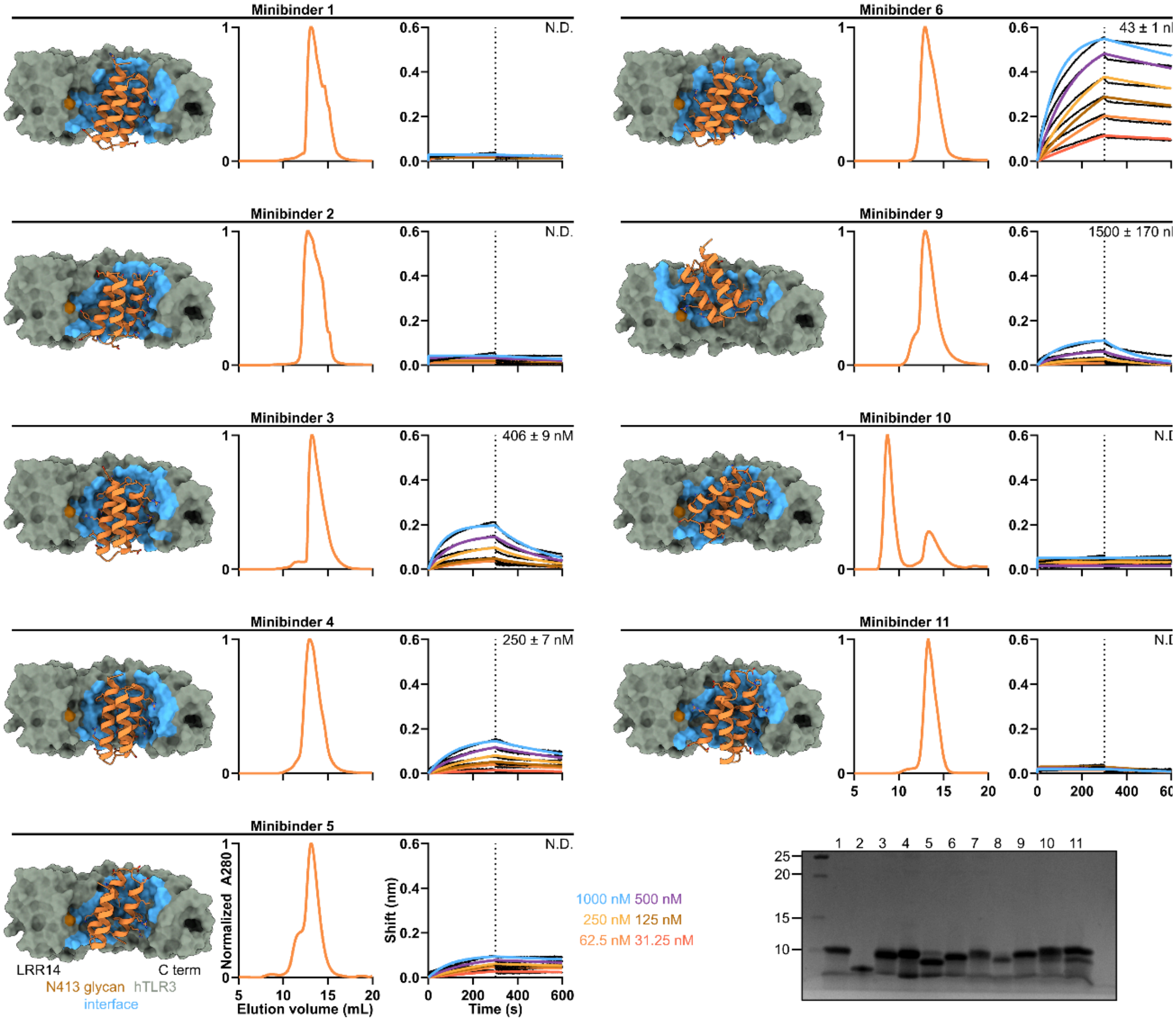

Extended Data Fig. 1: Experimental characterization of hits obtained by yeast display.

From left to right, design model, SEC, and BLI for each minibinder. K_D values are listed; N.D. indicates poor fit or no binding. *Bottom*, reducing SDS-PAGE of minibinders 1-11.

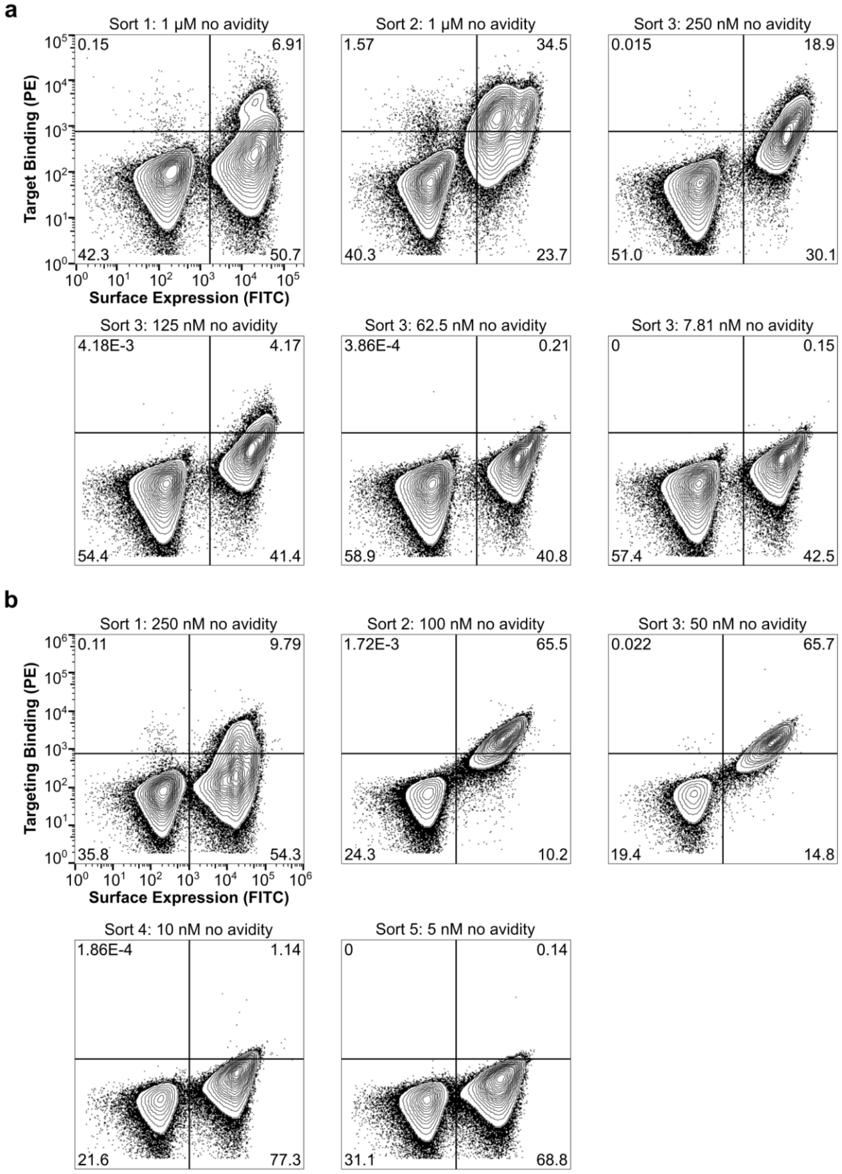

Extended Data Fig. 2: Affinity maturation of initial hits using yeast surface display.

a, Yeast displaying the SSM libraries for each design were pooled and incubated with fluorescently labeled hTLR3. Double positive cells were collected for sequencing and additional rounds of sorting for a total of 3 sorts. **b,** Yeast displaying the combinatorial libraries for each design were pooled and incubated with fluorescently labeled hTLR3.

Double positive cells were collected for sequencing and additional rounds of sorting for a total of 5 sorts.

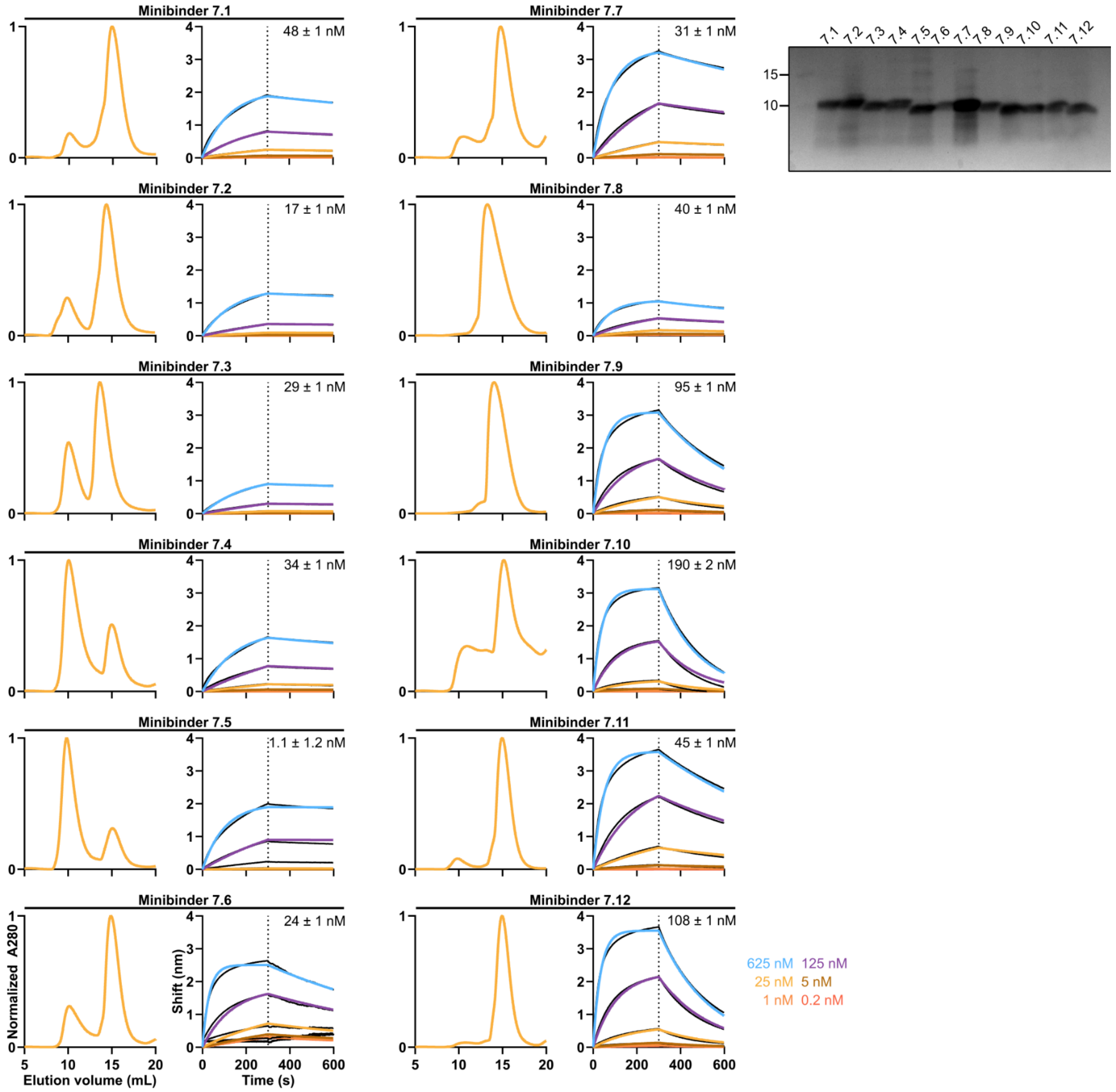

Extended Data Fig. 3: Biochemical and biophysical characterization of minibinder 7 variants.

Left, SEC, BLI, and *Right,* reducing SDS-PAGE of affinity-matured minibinders. K_D values are listed for each minibinder.

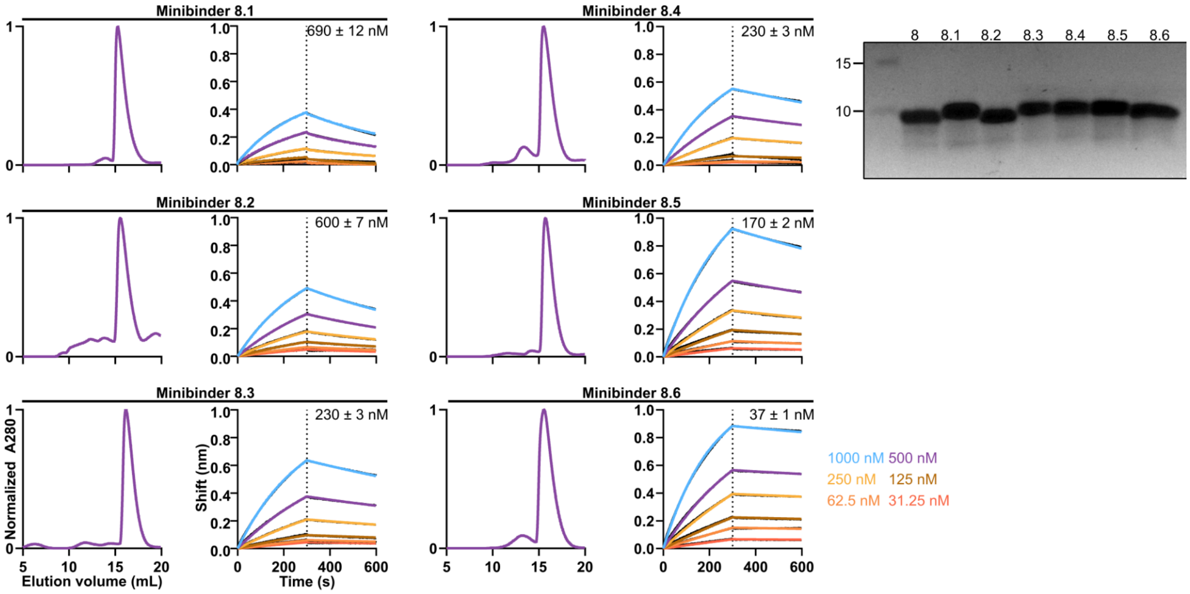

Extended Data Fig. 4: Biochemical and biophysical characterization of minibinder 8 variants.

Left, SEC, BLI, and *Right,* reducing SDS-PAGE of affinity-matured minibinders. K_D values are listed for each minibinder.

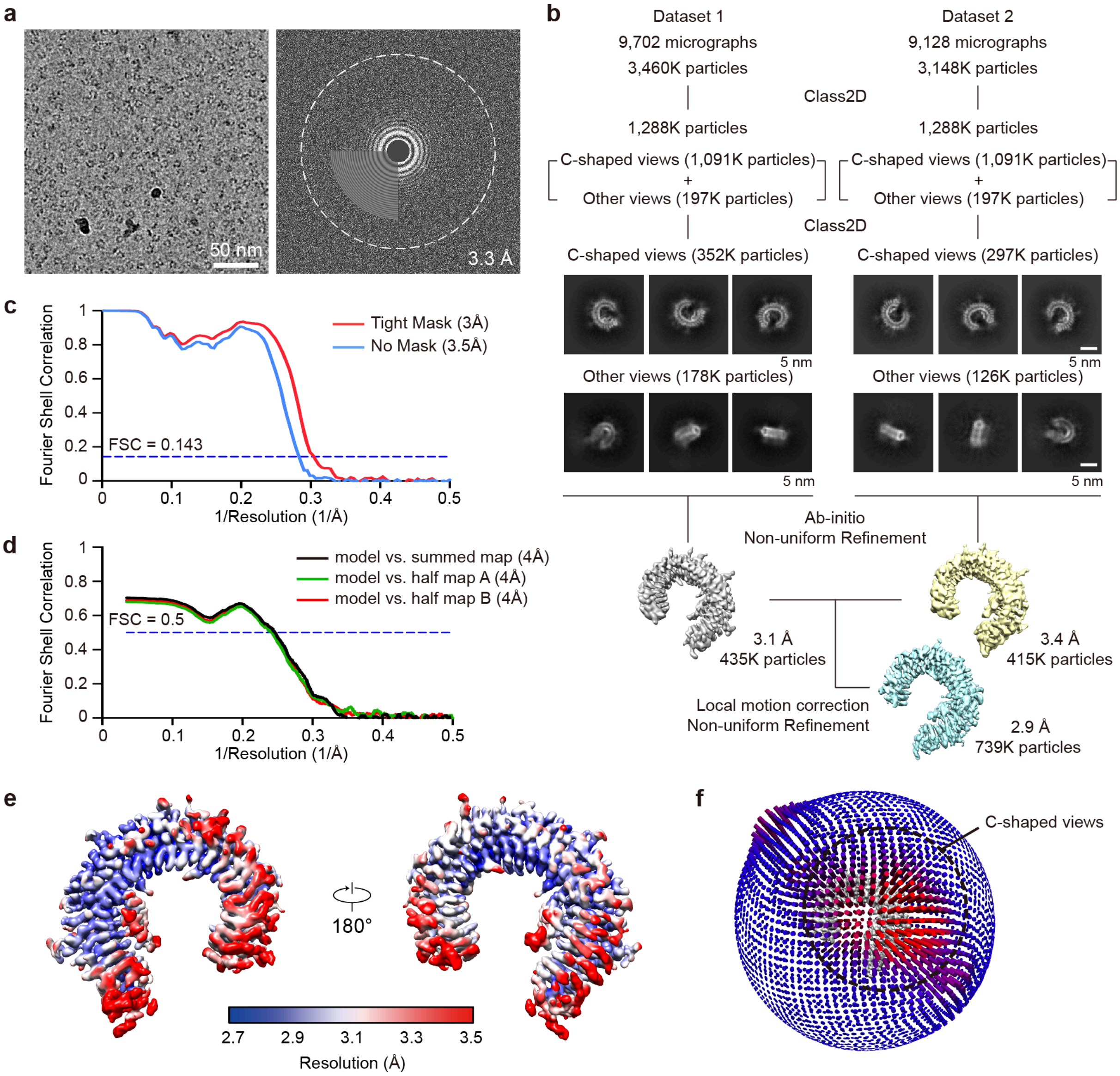

Extended Data Fig. 5: Cryo-EM analysis of TLR3/minibinder 7.7 complex.
a, Representative cryo-EM micrograph (left) and its Fourier transform (right). **b,** Data processing workflow of cryo-EM analysis and representative 2D class averages of the TLR3/minibinder 7.7 complex. **c,** Gold-standard Fourier shell correlation (FSC) between two independently refined half-maps in cryoSPARC (resolution cutoff at FSC = 0.143). **d,** FSC curves for cross-validation: model versus summed map (black), model versus half-map A (used in test refinement, green), and model versus half-map B (not used in test refinement, red). **e,** Final cryo-EM map colored by local resolution. **f,** Euler angle distribution of all particles used in the final 3D reconstructions. The height and color (from blue to red) of the cylinder bars are proportional to the number of particles in those views.

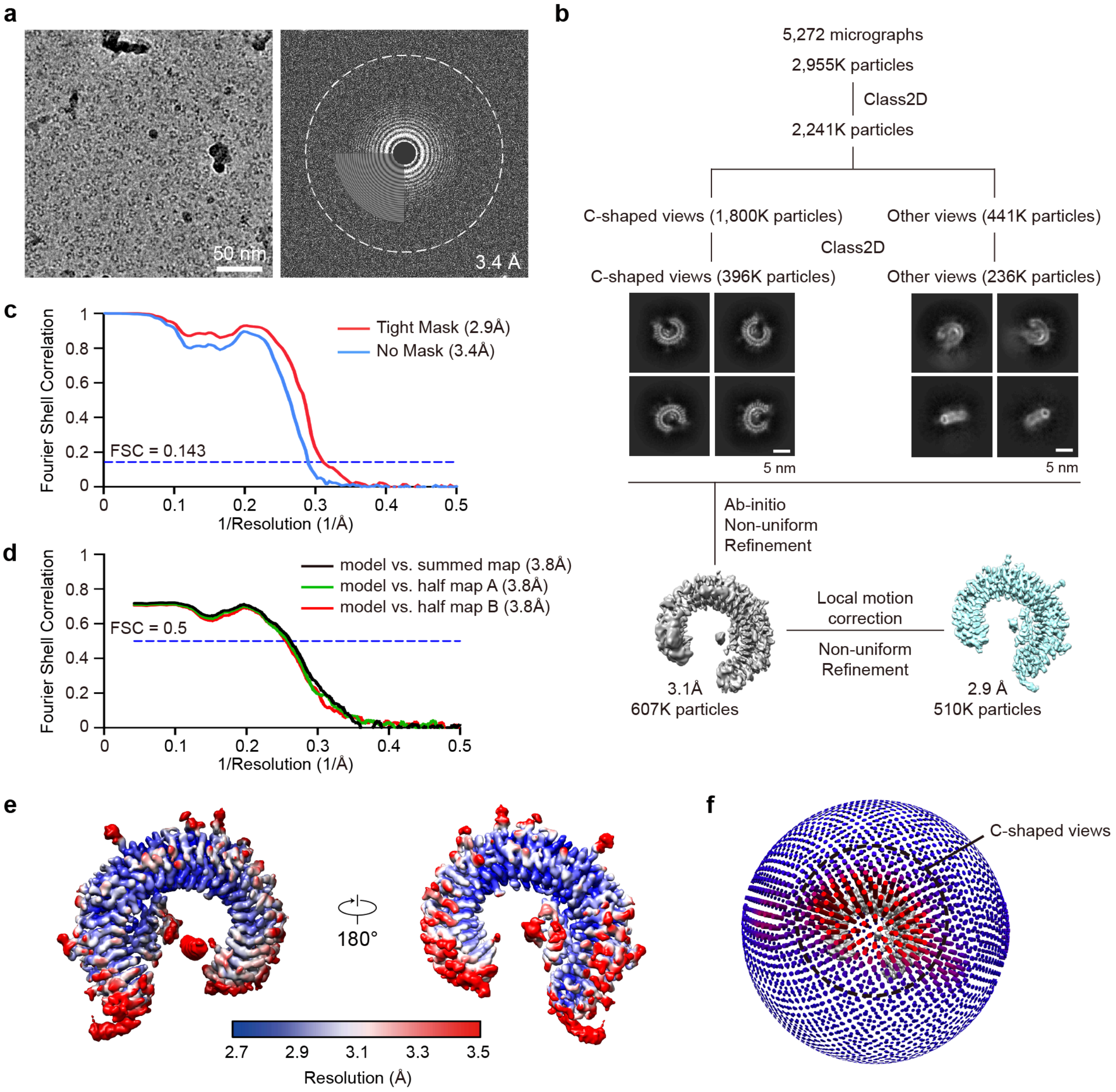

Extended Data Fig. 6: Cryo-EM analysis of TLR3/minibinder 8.6 complex.
a, Representative cryo-EM micrograph (left) and its Fourier transform (right). **b,** Data processing workflow of cryo-EM analysis and representative 2D class averages of the TLR3/minibinder 8.6 complex. **c,** Gold-standard Fourier shell correlation (FSC) between two independently refined half-maps in cryoSPARC (resolution cutoff at FSC = 0.143). **d,** FSC curves for cross-validation: model versus summed map (black), model versus half-map A (used in test refinement, green), and model versus half-map B (not used in test refinement, red). **e,** Final cryo-EM map colored by local resolution. **f,** Euler angle distribution of all particles used in the final 3D reconstructions. The

height and color (from blue to red) of the cylinder bars are proportional to the number of particles in those views.

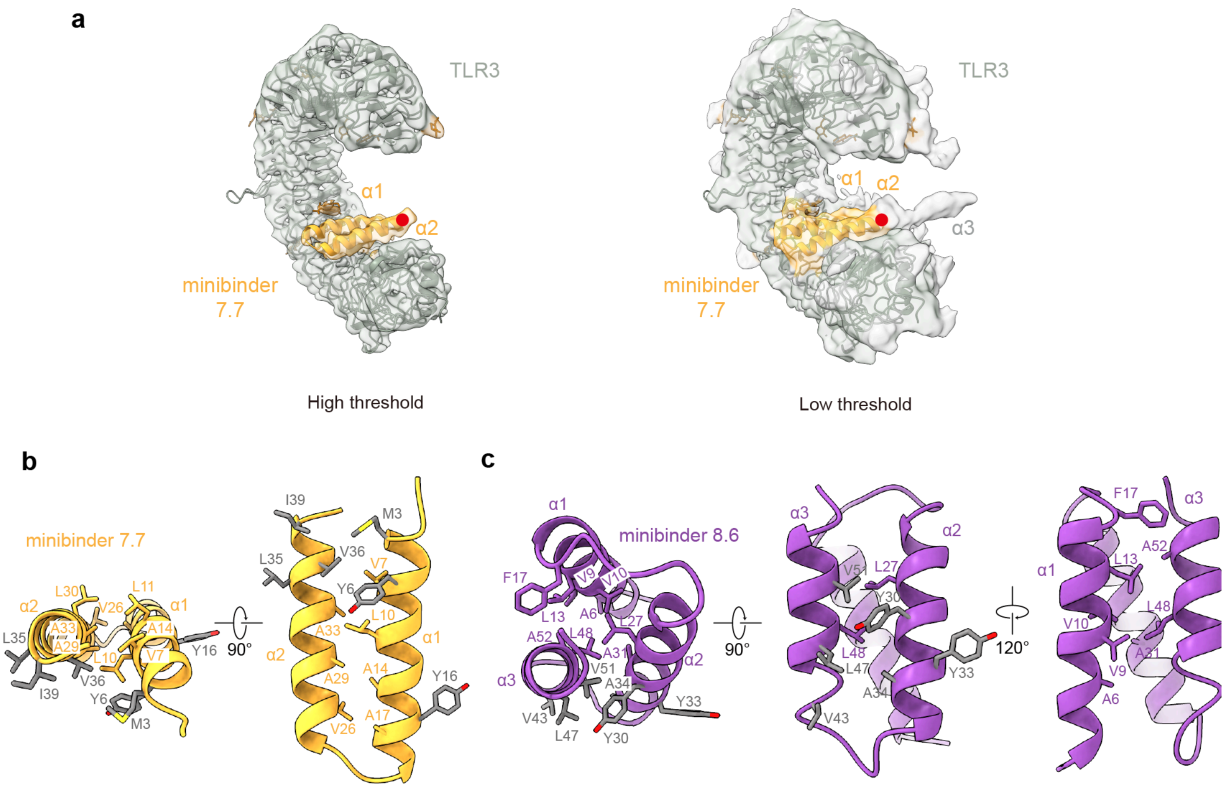

Extended Data Fig. 7: Helices and hydrophobic residues in minibinders.
a, Cryo-EM density for the third helix of minibinder 7.7 under high threshold (left, threshold = 0.2 σ) and low threshold (right, threshold = 0.08 σ). The C-terminal end of the second helix is marked with a red dot, and the potential density for the third helix is marked as α3. **b,c,** Hydrophobic residues in helices of minibinder 7.7 (**b**) and minibinder 8.6 (**c**). Interacting residues in the hydrophobic core are shown as yellow (minibinder 7.7) and purple (minibinder 8.6) sticks. Residues involved in hydrophobic interactions between each minibinder and TLR3 are colored in gray.

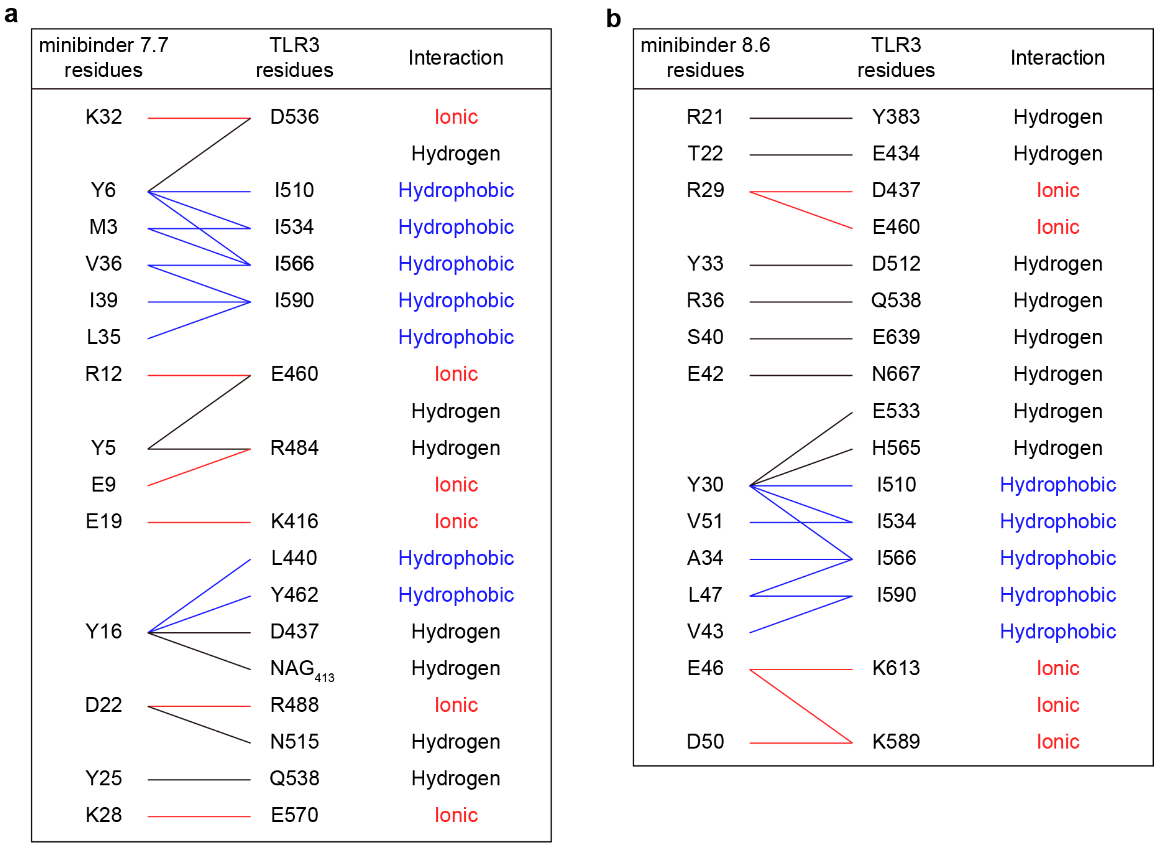

Extended Data Fig. 8: Interactions between minibinders and TLR3.
a,b, Residues making key interactions between TLR3 and minibinders 7.7 **(a)** and 8.6 **(b)** are provided, as well as the nature of each interaction.

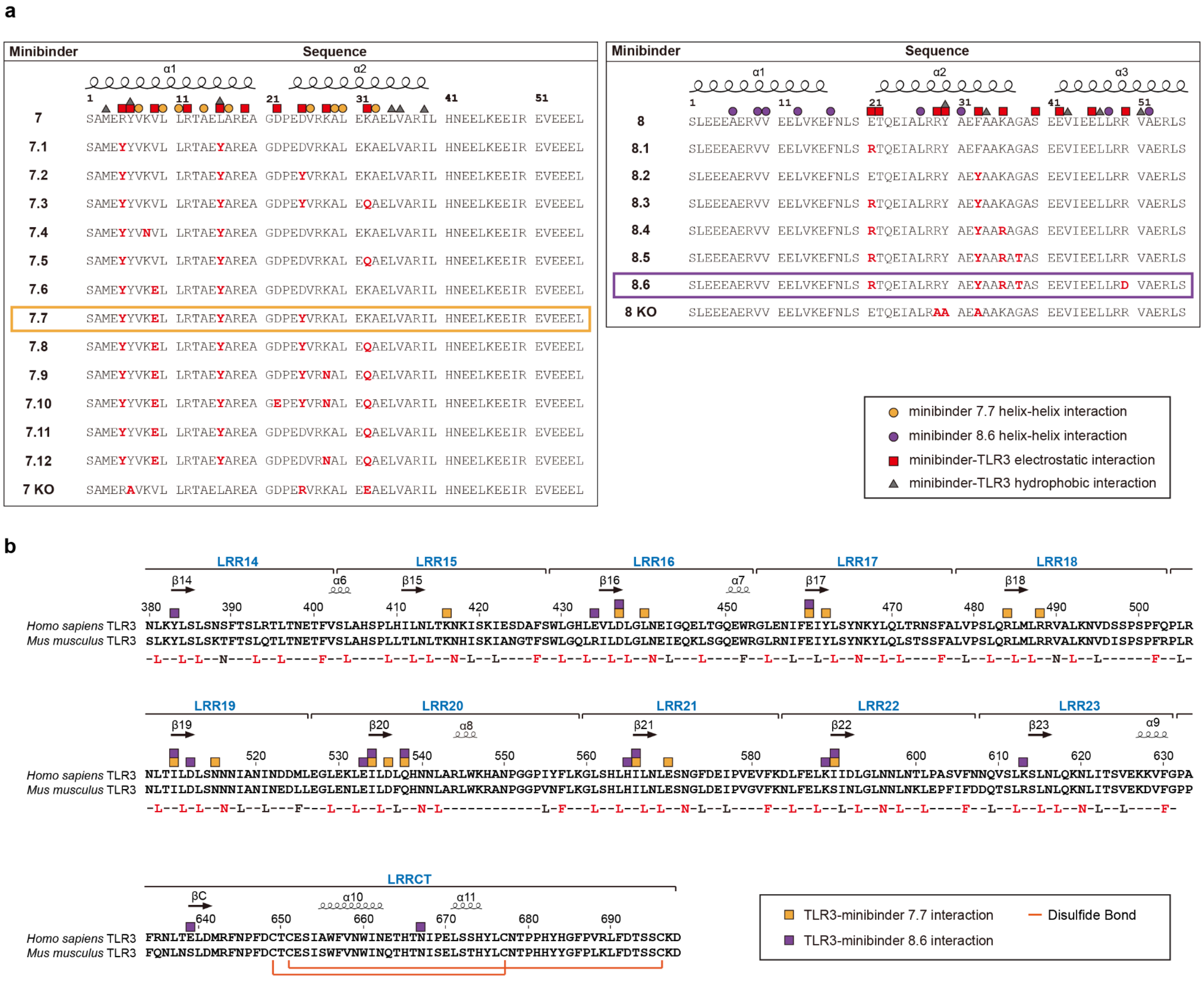

Extended Data Fig. 9: Sequence alignments of minibinder 7 and 8 derivatives and TLR3.

a, Amino acid sequence alignments of *left,* minibinder 7, and 7.1–12, and *right,* 7 KO or 8, 8.1–6, and 8 KO. Residues mutated from the parental designs 7 or 8 are colored red. α-helices are noted above the alignment. Red squares and gray triangles indicate residues involved in electrostatic and hydrophobic interactions in the structures of minibinders 7.7 or 8.6 and TLR3, respectively. Yellow and purple circles indicate helix-helix interacting residues in minibinders 7.7 and 8.6, respectively. **b,** Amino acid sequence alignment of human (*H. sapiens*, UniProt: O15455) and mouse (*M. musculus*, Uniprot: Q99MB1) TLR3. The LRR consensus sequence of TLR3 (xLxxLxxLxLxxNxLxxLxxxxFx) is provided under the LRR motif alignment, and residues conserved in both sequences are colored red. Domains (LRRNT, LRR1–LRR23 motif, and LRRCT) and secondary structure (arrows for β stands and helices for α-helices) elements are noted above the alignment. Yellow and purple squares indicate TLR3 residues interacting with minibinders 7.7 and 8.6, respectively. Disulfide bonds are also indicated by orange lines. The sequence alignment was created using T-Coffee (http://tcoffee.crg.cat)[101].

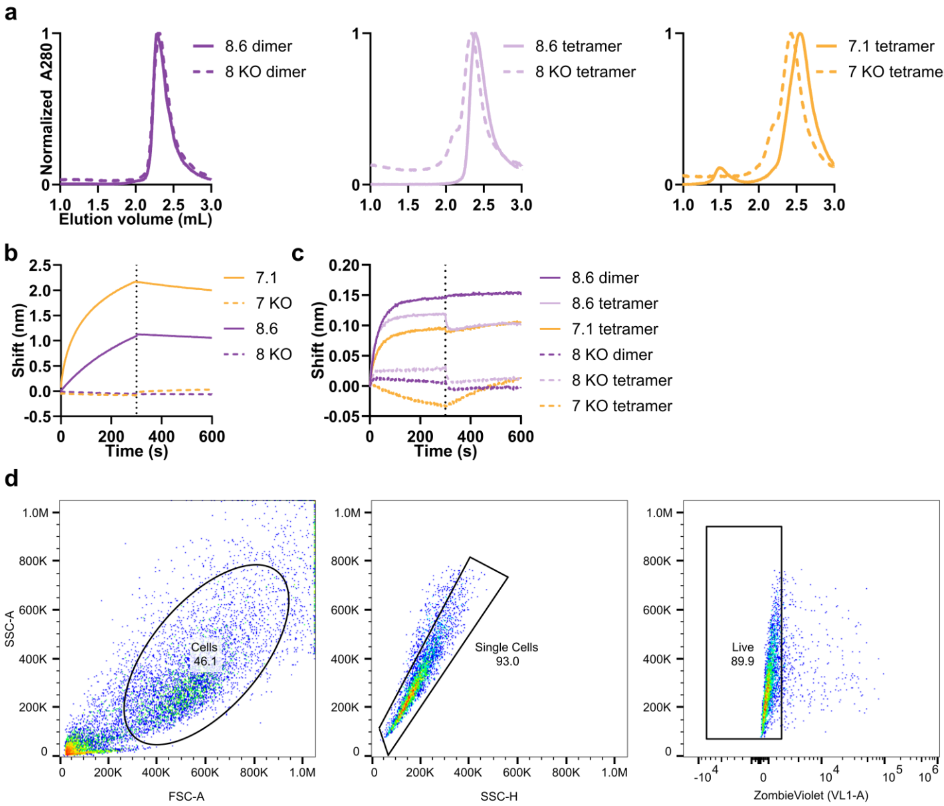

Extended Data Fig. 10: Characterization of multimers and gating strategy.

a, SEC of multimers. **b,c,** BLI of minibinder and knockout monomers (**b**) and multimers (**c**). **d,** Gating strategy for measuring GFP expression in HEK293-TLR3hi cells.

Supplementary Table 1. Amino acid sequences

Construct*	Amino Acid Sequence
1	DR[**V**/I][**L**/Y]RA[**A**/R]AELAF[**K**/R]NLRID[**V**/I/L/M]EENDPEEVR[**Q**/S/T/Y]NLR[**H**/R]LET[**L**/Y]ARVLNDPEIERLVEEVKELLG
2	DEVWRILAQ[**M**/I][**T**/N][**H**/S]I[**L**/K/N/S/Q][**S**/N]HIDDPEE[**A**/N/S]YEV[**S**/D/N]RLF[**L**/Y]RVYELNDPEYARRALERAEEL
3	DN[**F**/Y]RYY[**V**/A/G]E[**Q**/N/S/Y]LLR[**S**/H/N/T]AEL[**L**/E/S]LEEGDPE[**E**/Y]AE[**L**/N/Q/R/S][**A**/R/S]L[**R**/H][**S**/N/Q]AKTVAR[**L**/I/V]ENDEELRRLVEELERRL
4	DD[**I**/N/T]FE[**F**/W]YIKYLIE[**A**/Q/N/T]AK[**R**/Y]AYEE[**G**/I]DDEAAENDLR[**T**/H]ARSAARVLGDEELRRLIEELERKI
5	DLEELIREARELLEKGNPYEAAK[**V**/Y]VLE[**A**/S]IHLAI[**Q**/M]K[**D**/R]DDE[**L**/R][**F**/I/L/M/S]LEAWRLYREILG
6	S[**A**/N/S/T]VELYLELLERS[**L**/M/T]R[**L**/F/Y]A[**V**/L]EAGDPEDAER[**I**/D][**L**/K]R[**K**/H/T]ARQIARVFNDPELEEIVERMEEILK
7	S[**A**/I/V]ME[**R**/H/Y]YVK[**V**/E]LLRTAE[**L**/Y]AREAG[**D**/E/H]PE[**D**/E/H/Y]VR[**K**/N/S/T][**A**/L]LE[**K**/F/Q]AE[L/M]VARILHNEELKEEIREVEEEL
8	SLEEEAERVVEELVKEFNLSET[**Q**/H]EI[**A**/H/Y]LRRY[**A**/E/H/R/Q]E[**F**/Y]AA[**K**/R]AGASEEVIEEL[**L**/V]RRVAERLS
9	DELERLAEEIVERLVKEYNLDFKQKLRLRIIAESLLEHGFDEELIELLLERDARRLS
10	DEELREVVERLVEKFQLSEEAKKVLEEVVKRLEERGFDEKLAKLRLYLVAARLSVEL
11	S[**D**/E]EA[**A**/Y]RIARE[**I**/V]LKLAEYAIKTDDPEALRLYNEAK[**N**/R]LL[**S**/H/N/R]EAEAKNSEEVLKKVEEVVRKAQKNVS
7.1	SAMEYYVKVLLRTAEYAREAGDPEDVRKALEKAELVARILHNEELKEEIREVEEEL
7.2	SAMEYYVKVLLRTAEYAREAGDPEYVRKALEKAELVARILHNEELKEEIREVEEEL

7.3	SAMEYYVKVLLRTAEYAREAGDPEYVRKALEQAELVARILHNEELKEEIREVEEEL
7.4	SAMEYYVNVLLRTAEYAREAGDPEDVRKALEKAELVARILHNEELKEEIREVEEEL
7.5	SAMEYYVKVLLRTAEYAREAGDPEDVRKALEQAELVARILHNEELKEEIREVEEEL
7.6	SAMEYYVKELLRTAEYAREAGDPEDVRKALEKAELVARILHNEELKEEIREVEEEL
7.7	SAMEYYVKELLRTAEYAREAGDPEYVRKALEKAELVARILHNEELKEEIREVEEEL
7.8	SAMEYYVKELLRTAEYAREAGDPEYVRKALEQAELVARILHNEELKEEIREVEEEL
7.9	SAMEYYVKELLRTAEYAREAGDPEYVRNALEQAELVARILHNEELKEEIREVEEEL
7.10	SAMEYYVKELLRTAEYAREAGEPEYVRNALEQAELVARILHNEELKEEIREVEEEL
7.11	SAMEYYVKELLRTAEYAREAGDPEDVRKALEQAELVARILHNEELKEEIREVEEEL
7.12	SAMEYYVKELLRTAEYAREAGDPEDVRNALEQAELVARILHNEELKEEIREVEEEL
7 KO	SAMERAVKVLLRTAELAREAGDPERVRKALEEAELVARILHNEELKEEIREVEEEL
8.1	SLEEEAERVVEELVKEFNLSRTQEIALRRYAEFAAKAGASEEVIEELLRRVAERLS
8.2	SLEEEAERVVEELVKEFNLSETQEIALRRYAEYAAKAGASEEVIEELLRRVAERLS
8.3	SLEEEAERVVEELVKEFNLSRTQEIALRRYAEYAAKAGASEEVIEELLRRVAERLS

8.4	SLEEEAERVVEELVKEFNLSRTQEIALRRYAEYAARAGASEEVIEELLRRVAERLS
8.5	SLEEEAERVVEELVKEFNLSRTQEIALRRYAEYAARATASEEVIEELLRRVAERLS
8.6	SLEEEAERVVEELVKEFNLSRTQEIALRRYAEYAARATASEEVIEELLRDVAERLS
8 KO	SLEEEAERVVEELVKEFNLSETQEIALRAAAEAAAKAGASEEVIEELLRRVAERLS
tetramer	**[BINDER]**GGSGGSGGSGGSGGSG[**BINDER]**GGSGGSGGSGGSGGSG[**BINDER]**GGSGGSGGSGGSGGSG[**BINDER]**
dimer	GSHENKQVEEILRLEKEIEDLQRMKERQELSLTEASLQKLQLEDKVEELLSKNYHLENEVARLKKLVGEGGSGGSGGSGGSGGSGGSGGSGGS[**BINDER]**
TLR3 ectodomain	MLLVNQSHQGFNKEHTSKMVSAIVLYVLLAAAAHSAFAKCTVSHEVADCSHLKLTQVPDDLPTNITVLNLTHNQLRRLPAANFTRYSQLTSLDVGFNTISKLEPELCQKLPMLKVLNLQHNELSQLSDKTFAFCTNLTELHLMSNSIQKIKNNPFVKQKNLITLDLSHNGLSSTKLGTQVQLENLQELLLSNNKIQALKSEELDIFANSSLKKLELSSNQIKEFSPGCFHAIGRLFGLFLNNVQLGPSLTEKLCLELANTSIRNLSLSNSQLSTTSNTTFLGLKWTNLTMLDLSYNNLNVVGNDSFAWLPQLEYFFLEYNNIQHLFSHSLHGLFNVRYLNLKRSFTKQSISLASLPKIDDFSFQWLKCLEHLNMEDNDIPGIKSNMFTGLINLKYLSLSNSFTSLRTLTNETFVSLAHSPLHILNLTKNKISKIESDAFSWLGHLEVLDLGLNEIGQELTGQEWRGLENIFEIYLSYNKYLQLTRNSFALVPSLQRLMLRRVALKNVDSSPSPFQPLRNLTILDLSNNNIANINDDMLEGLEKLEILDLQHNNLARLWKHANPGGPIYFLKGLSHLHILNLESNGFDEIPVEVFKDLFELKIIDLGLNNLNTLPASVFNNQVSLKSLNLQKNLITSVEKKVFGPAFRNLTELDMRFNPFDCTCESIAWFVNWINETHTNIPELSSHYLCNTPPHYHGFPVRLFDTSSCKDSAGGSHHHHHHGGSGLNDIFEAQKIEWHE

---

* For minibinders 1-11, the amino acids encoded by degenerate codons in the combinatorial libraries are listed in brackets, with the original amino acid bolded.

Supplementary Table 2. Association and dissociation rates for TLR3/minibinder interactions, determined by BLI

Minibinder	K_{on} ($M^{-1}s^{-1}$)	K_{off} (s^{-1})
1	N.D.*	N.D.
2	N.D.	N.D.
3	1.1E+04	4.5E-03
4	6.9E+03	1.7E-03
5	N.D.	N.D.
6	1.1E+04	4.9E-04
7	4.8E+03	2.1E-03
8	2.5E+03	3.0E-03
9	4.1E+03	6.3E-03
10	N.D.	N.D.
11	N.D.	N.D.
7.1	7.9E+03	3.4E-04
7.2	9.3E+03	1.6E-04
7.3	8.0E+03	2.3E-04
7.4	1.0E+04	3.6E-04
7.5	1.6E+04	1.8E-05
7.6	5.0E+04	1.2E-03
7.7	1.9E+04	5.9E-04
7.8	2.0E+04	7.7E-04
7.9	2.9E+04	2.7E-03
7.10	3.0E+04	5.7E-03
7.11	3.0E+04	1.4E-03
7.12	4.0E+04	4.4E-03
8.1	2.8E+03	1.9E-03
8.2	2.1E+03	1.3E-03

8.3	2.9E+03	6.5E-04
8.4	2.9E+03	6.5E-04
8.5	3.3E+03	5.6E-04
8.6	4.5E+03	1.7E-04

*N.D. indicates no binding data.

Supplementary Table 3. Cryo-EM data collection, refinement, and validation statistics

	TLR3/minibinder 7.7	**TLR3/minibinder 8.6**
Data collection and processing		
Magnification	130,000	130,000
Voltage (kV)	300	300
Electron exposure ($e^-/Å^2$)	68.9	69.8
Defocus range (μm)	-0.8 – -2.2	-0.8 – -2.0
Pixel size (Å)	0.664	0.664
Symmetry imposed	C1	C1
Initial particle images (no.)	6,608,485	2,955,749
Final particle images (no.)	739,755	510,475
Map resolution (Å)	2.88	2.88
FSC threshold	0.143	0.143
Refinement		
Initial model used	AF2 prediction	AF2 prediction
Map resolution (Å)	2.88	2.88
FSC threshold	0.143	0.143
Map sharpening B factor ($Å^2$)	0	0
Model composition		
Non Hydrogen atoms	5,845	5,990
Protein residues	703	719
Ligands	14	15
B factors ($Å^2$)		
Protein	75.39	64.40
Ligand	77.43	70.91
R.m.s. deviations		
Bond lengths (Å)	0.26	0.26

Bond angles (°)	0.51	0.51
Validation		
MolProbity score	2.33	2.15
Clashscore	11	11
Poor rotamers (%)	0	0
Ramachandran plot		
Favored (%)	88	87
Allowed (%)	12	13
Outliers (%)	0	0

Chapter 3. Stabilizing flagellin, a TLR5 agonist

Abstract

Flagellin is one of the only protein-based TLR agonists. Yet, flagellin is prone to aggregation and degradation which makes it an unsuitable adjuvant candidate. Here, we describe two efforts to stabilize flagellin. Ultimately, we tested stabilized versions of flagellin *in vivo* with the SARS-CoV-2 receptor-binding domain as an antigen, and saw no immunological impact from stabilized or native flagellin.

Introduction

Toll-Like Receptor 5 (TLR5) is a pattern recognition receptor that is activated by the bacterial protein flagellin[14]. TLR5 activation leads to the upregulation of NF-κB signaling[102]. Flagellin is the best studied TLR protein agonist and its immune stimulating properties make it a potential vaccine adjuvant candidate[103]. However, flagellin is prone to aggregation and degradation, limiting its translational impact due to manufacturing difficulties.

Flagellin consists of 2-4 domains (D0, D1, D2, and D3) (**Fig. 3a**). TLR5 binds to a conserved region in the D1 domain[104]. D2 and D3 are variable and absent in some species of bacteria[105]. The D0 domain is responsible for aggregation, as it self-assembles and forms an 11-mer filament[103,71,106]. The C-terminus of the D0 domain is also susceptible to degradation[107]. Previous attempts at stabilization of flagellin have included an entire deletion or truncation of the D0 domain, however this leads to a decrease in TLR5 signaling[107]. Structural stabilization of the D0 domain using disulfides has been used to stabilize flagellin[71]. There is still room for improvement in thermal stability and general stability.

Here, I describe two attempts of further stabilizing flagellin using protein design. The first method focuses on maintaining the key flagellin-TLR5 residues in D1 and rebuilding new helices around these residues- a “mimetic” approach. The second method focuses on truncating D2 and D3 and stabilizing D0 with ProteinMPNN[108], a deep learning based design method.

Results

Computational design of flagellin mimetics

In our first approach, we used the Idealizer[50] design pipeline to build a flagellin mimetic based on D1. This strategy maintains the critical residues of the D1 domain, but the rest of the structure is *de novo*- leading to potentially more stable variants. Critical residues were chosen based on the flagellin-TLR5 interface and alanine scanning of the interface[14,109]. A fourth helix was added to some designs to further stabilize flagellin. It is important to note that this design is done in the context of the target receptor. At the time, the only structure of TLR5 in the PDB was zebrafish TLR5 (drTLR5), which is only ~40% similar in sequence to human TLR5 (hTLR5) (Uniprot 060602, F8W3J5). Now, there are AlphaFold predicted structures of human and mouse TLR5 (mTLR5).

100s of designs were made in the context of drTLR5 and filtered by ddG and interface SASA. 47 designs were screened for binding against 1 μM drTLR5 using yeast surface display (**Fig. 1a**). 5 hits bound to drTLR5 (**Fig. 1b**). These designs did not bind to hTLR5 or mTLR5. Error-Prone PCR was performed on the 47 designs to introduce random mutations that might rescue binding. Binding to mTLR5 was rescued **(Fig. 1c**). Predictions of these mutations showed they caused partial unfolding of the designs (**Fig. 1d**). Thus, it seemed like the cross-reactive variants might be poorly behaved.

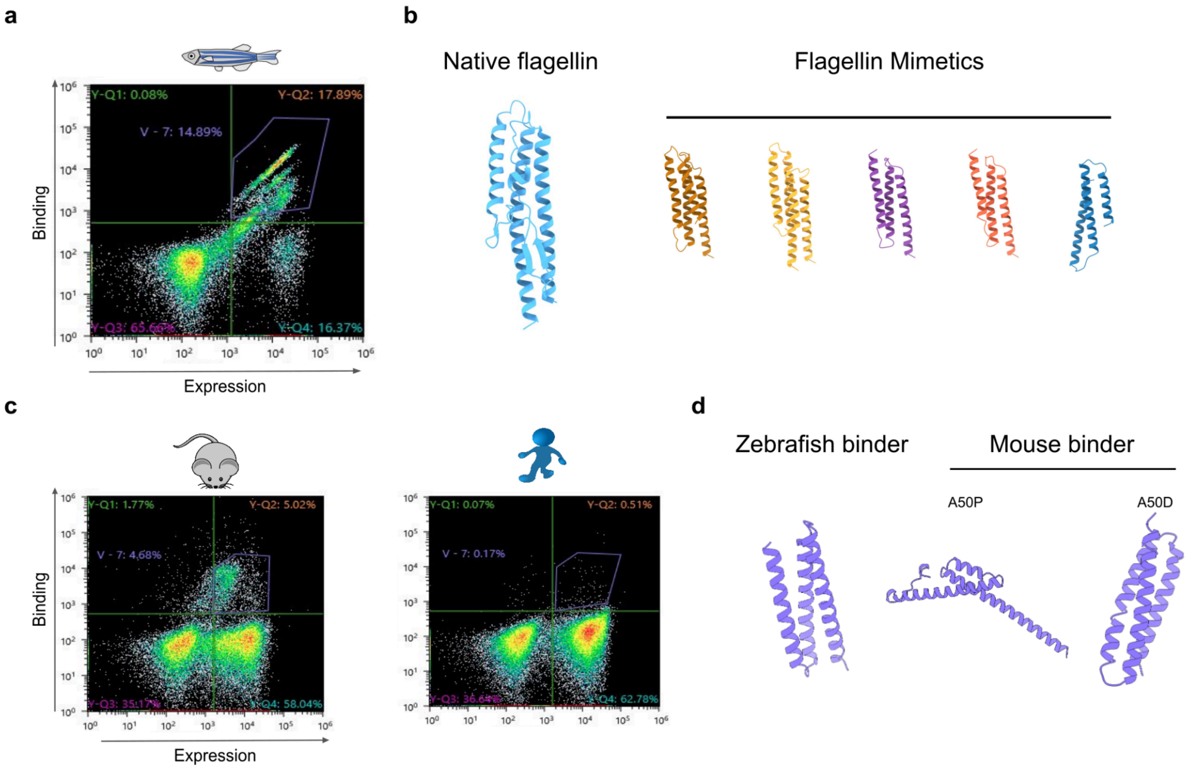

Fig. 1. Screening “idealized” flagellin

a, 47 designs were sorted against drTLR5. **b,** 5 hits were identified via colony PCR. **c,** Designs were cross-reactive to mTLR5. **d,** Mutations at residue 50 in Design 29 rescued binding to mTLR5 but are predicted to affect folding.

It was unclear why there was no binding to hTLR5, despite native flagellin being cross-reactive to zebrafish/human/mice. We performed an additional design campaign of flagellin mimetics against a homology model of hTLR5. We also made *de novo* minibinders against hTLR5, following the same pipeline described in Chapter 2. Both of these campaigns yielded inconclusive results. We began to have doubts that the hTLR5 ectodomain was properly folded- so we further characterized it.

The TLR5 ectodomain is notoriously difficult to make[110] and we were unable to produce it in house. At the time this work was carried out, one company, Invivogen, sold hTLR5-FC. Native flagellin readily bound to mTLR5-FC via BLI, but had only low levels of binding to purchased hTLR5-FC (**Fig. 2a)**. Additionally, when visualizing mTLR5-FC with negative stain EM, the receptor shows the canonical horseshoe shapes of TLRs. However, hTLR5-FC had a heterogeneous mixture of an IgG antibody and the TLRs (**Fig. 2b**). We deemed hTLR5-FC not reliable to use and thus we had no source of human protein to screen designs against.

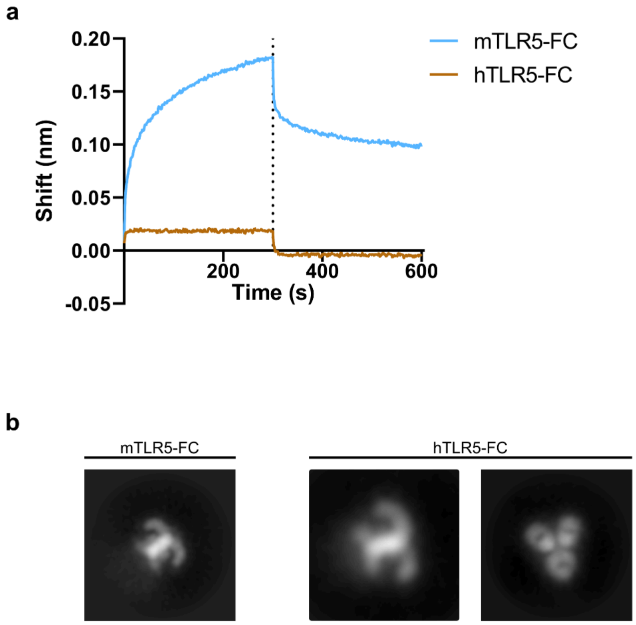

Fig. 2. Characterizing recombinant human TLR5.

a, Biotinylated flagellin is loaded onto streptavidin sensors. Binding signal is clear to mTLR5-FC but not hTLR5-FC. **b,** Negative stain micrographs of mTLR5-FC and hTLR5-FC. Human TLR5 has a heterogeneous population of TLR and an unknown IgG.

Computational design of stabilized flagellin

Our previous design methods were all performed in the context of the receptor. Due to unreliable hTLR5, we had to stabilize flagellin without disrupting the TLR5-flagellin interface. Additionally, we needed to develop a new way to screen designs. Protein MPNN has been used to design new protein sequences that are highly stable, while maintaining the original backbone[111]. Here, we use Protein MPNN to stabilize flagellin (**Fig. 3a**).

The D0 domain is known to be important for TLR5 signaling. However, it is unknown which of the 4 faces of the D0 contributes to signaling. Each design kept 1 face of D0 while the remaining 3 faces were altered to introduce less hydrophobic residues. All residues on D1 responsible for binding to flagellin were conserved on at least one of two potential binding sites. About half of the designs were derived from *Salmonella enterica* flagellin and the other half were derived from *Bacillus subtilis*. Designs 1 and 2 are most similar to previously described stabilizations in literature.

Designs express readily and activate TLR5

We expressed 24 designs with a C-terminal His6 tag in *E.coli* and purified them by immobilized metal affinity chromatography (IMAC) and size exclusion chromatography (SEC). Multiple designs showed truncation products or did not express (**Fig. 3b**). Designs were screened for TLR5 activation using HEK-Blue™ mouse TLR5 cells, which have a NF-κB reporter (**Fig. 4**). The majority of the expressing designs signaled similarly to native flagellin at 1000 ng/mL. To confirm that the NF-κB signaling was TLR5 specific, designs were tested in Ramos-Blue™ which has a NF-κB reporter but does not express TLR5. The designs did not signal in this assay (Data not shown). Designs were further characterized in a dilution series in the cell assay (**Fig. 5a**). Many of the designs followed the same signaling pattern as native flagellin.

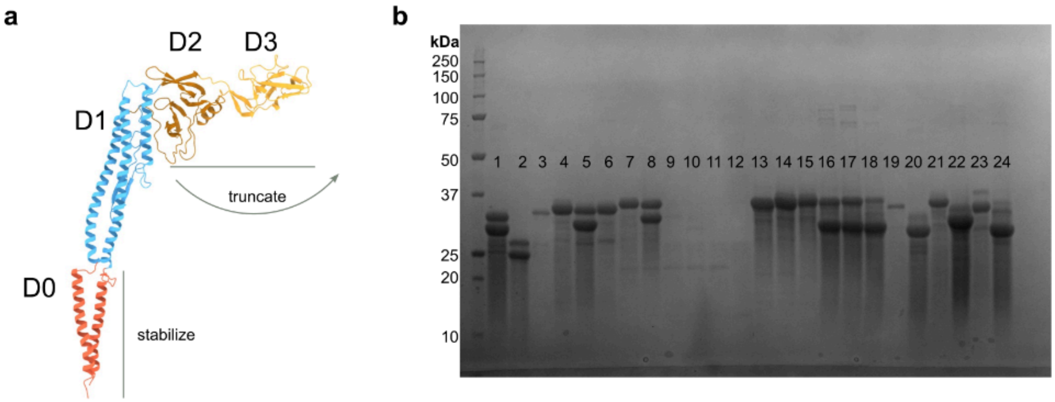

Fig. 3. MPNN expression

a, Flagellin (PDB: 1UCU). D2 and D3 were truncated. D0 was modified using MPNN.
b, Reducing SDS-PAGE of purified designs.

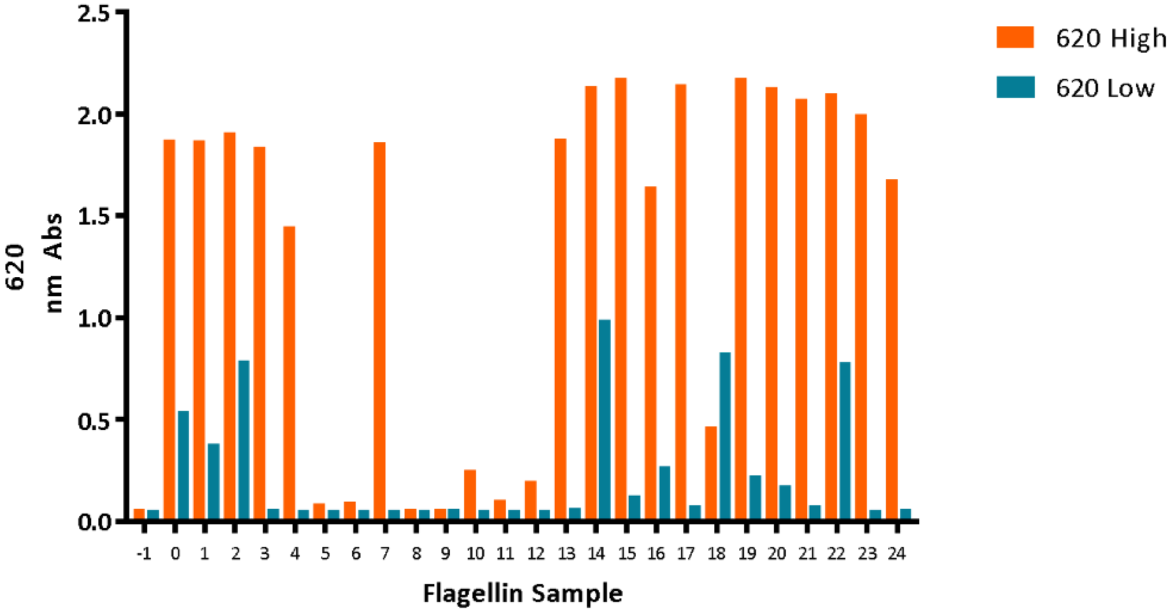

Fig. 4. Stabilized flagellin leads to native levels of NF-κB activation

-1 indicates the negative control LPS. 0 indicates purchased Flagellin (Rec Fla-st). All other numbers correspond to design numbers. The high concentration is 1000 ng/mL and the low is 5 ng/mL

Designs were displayed on a protein nanoparticle

Flagellin has been displayed multivalently on ferritin, VLPs, and gold nanoparticles to increase activation[112,71,112113]. Previously, our lab has effectively used a two component protein-based nanoparticle to display SARS-CoV-2 RBD[114].

Flagellin designs were displayed on the trimeric component of the nanoparticle and assembled with bare pentamer[115]. We tested activation of stabilized flagellin fused to the trimer and full cage (**Fig. 5b**). Surprisingly, the full nanoparticle was not always more potent than the trimer.

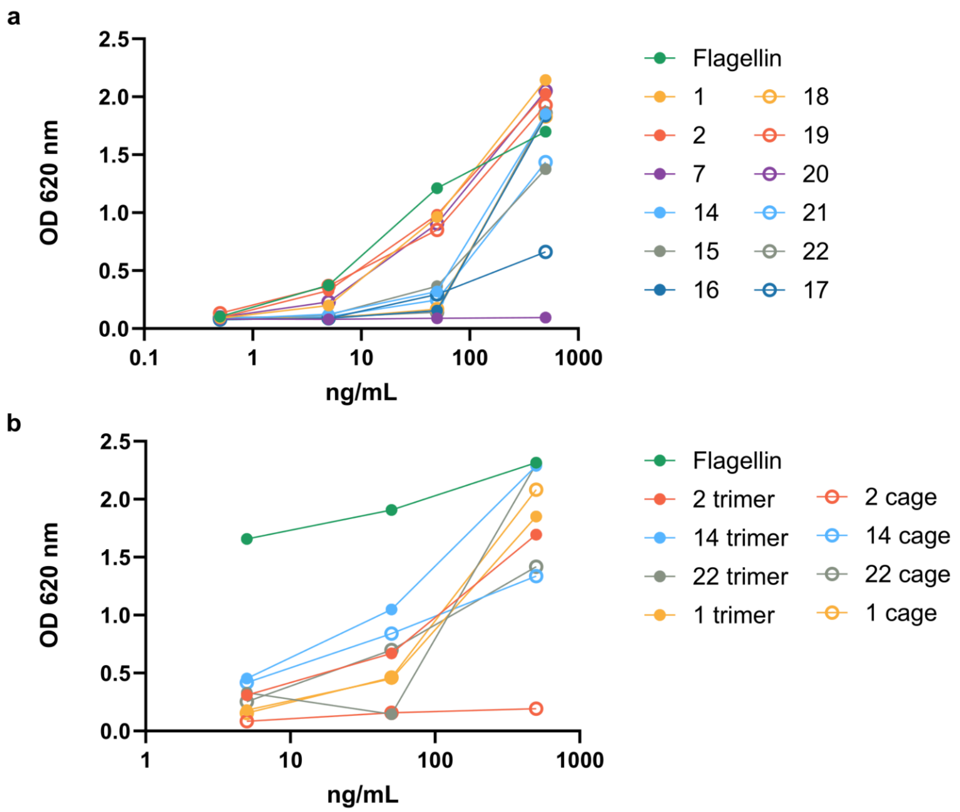

Fig. 5. Dilution series of stabilized flagellin

a, Stabilized flagellin was tested for activation in a 4 point dilution series. **b,** Trimers and full cages genetically fused to stabilized flagellin were tested for activation in a 3 point dilution series.

Thermostability of stabilized flagellin

Designs were characterized for thermostability using a SYPRO thermal shift assay (**Fig. 6**). Native flagellin had a melting temperature around 40℃. Designs 1 and 2, which are derived from literature, show an increase in melting temperature to around 45℃. All other designs tested show an improvement to 50-60℃.

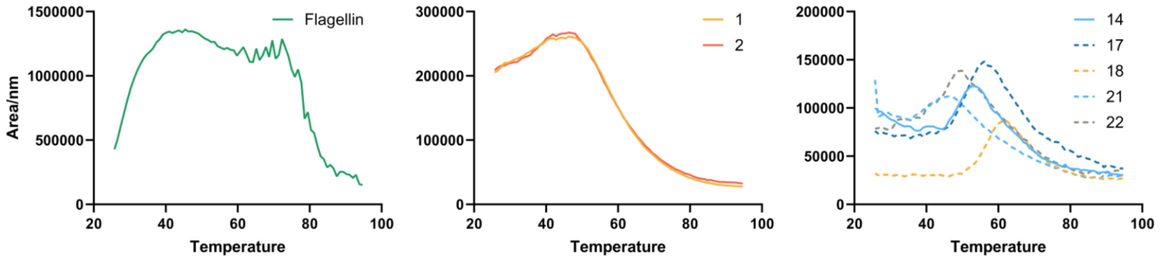

Fig. 6. MPNN stabilized flagellin have increased melting temperatures.

Left Flagellin has a relatively low melting temperature. *Center* This is improved slightly with the introduction of disulfides. *Right* The melting temperature is further increased with MPNN stabilized designs.

Adjuvanticity was tested in mice

Various valencies of flagellin on the nanoparticle were tested (12.5, 25, 50, and 100) and tested in HEK-Blue™ mouse TLR5 cells. 50% valency had a similar signaling to 100% valency and was used for *in vivo* studies. SARS-CoV-2 RBD trimers were co-assembled with flagellin trimers into 50/50 nanoparticles. Nanoparticle formation was confirmed using size exclusion chromatography, dynamic light scattering, and electron microscopy **(Fig. 7a**). Additionally, the antigen was confirmed to not disrupt signaling using HEK-Blue™ mouse TLR5 cells.

We evaluated the immunogenicity of our flagellin particles by measuring antigen-specific titers in serum after immunizing 11 BALB/c mice twice with adjuvanted nanoparticles four weeks apart (**Fig. 7b**). Addavax™, an oil-in water MF59 like emulsion, was used as positive control for adjuvanticity. Two weeks post-prime, the highest levels of antigen-specific antibodies were observed in the sera of animals that received Addavax™. Two weeks post-boost, highest levels of antigen-specific antibodies were again observed in the sera of animals that received Addavax™. No significant difference was seen in the sera of animals that received the flagellin nanoparticles.

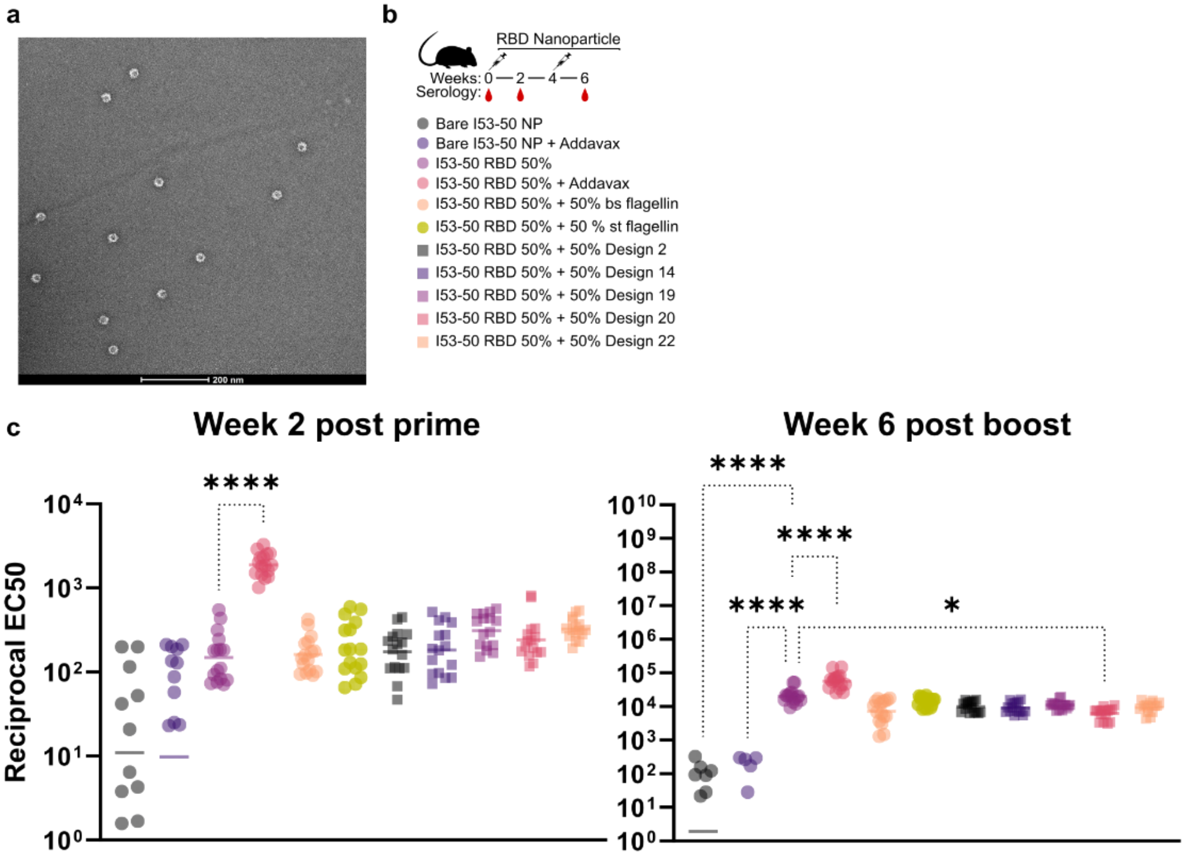

Fig. 7. Anti-Hexapro responses elicited by adjuvanted RBD nanoparticles.

a, Negative stain micrographs depicting nanoparticles. **b,** Study design and groups. Groups of BALB/c mice were immunized at weeks 0 and 4, and serum was obtained at weeks 0, 2, and 6. **c,** Serum antibody titers against SARS-CoV2-HexaPro.

Discussion

This chapter presents two approaches to stabilize flagellin, a potent TLR5 agonist, which could potentially serve as a vaccine adjuvant.

The first approach involved the design of D1 mimetics that maintain critical residues for TLR5 binding while incorporating *de novo* structural elements to potentially enhance stability. In hindsight, this design was done in the context of zebrafish TLR5, which is not highly conserved to human or mouse. The model was a zebrafish-VLR hybrid which further decreased the similarity.

A significant challenge encountered during the study was sourcing reliable human TLR5 ectodomain. This difficulty led to the start of another project in the lab that focuses on stabilizing the TLR2 and TLR5 ectodomains with ProteinMPNN (led by Cameron Criswell).

We moved to a receptor-independent approach, where we stabilized D0 with MPNN. Despite the successful stabilization of flagellin and its demonstrated activity *in vitro*, we found no significant immunological impact *in vivo* when tested with SARS-CoV-2 RBD as an antigen.

After completing our study, we examined a paper with RBD on ferritin and different TLR agonists as adjuvants. Flagellin did not increase RBD-specific IgGs, but Pam2CSK4 (a TLR2/6 agonist) did[116]. Work in the field shows flagellin increased IgG responses against HA when co-displayed on a nanoparticle with HA[112]. It is possible that RBD was not the correct antigen to use with TLR5. It is also possible that our nanoparticle went to cells that did not express TLR5.

In summary, we used innovative strategies to stabilize flagellin that showed promising results *in vitro*. However, there was a lack of significant immunological impact *in viv*o which underscores the challenges and complexities associated with the development of effective protein-based vaccine adjuvants. Further research is needed to address these challenges and optimize the design and formulation of flagellin-based adjuvants for potential clinical applications.

Acknowledgements

Thank you to Naveen Jasti for leading the design work described here. Thank you to Jung Ho Chun for mentorship on the Idealizer pipeline. Thank you to Anika Gupta for helping test the stabilized designs in the lab. Thank you to Elizabeth Sorberg and other IPD In Vivo Core members for doing the mouse studies. Thank you to IPD core members, Adian Valdez and others, for making RBD-50A. Thank you to Craig Dobbins for maintaining cells for assays. Thank you to Suna Chen for helping with ELISAs.

Materials and Methods

Computational Design

Flagellin mimetics were designed as outlined in ref.[50]. BundleGridSampler mover was used to generate a 4th helix in a subset of designs[117]. ProteinMPNN was used to redesign three of four faces of D0 in the second approach[50,108].

Yeast surface display

As described in Chapter 2.

Protein purification

Zebrafish TLR5 was purchased as a custom order from Wuxi Biologics. Mouse TLR5-Fc (R&D Systems, #7915-TR-025) and Human TLR5-Fc (Invivogen, #fc-htlr5-2) were purchased. Recombinant flagellin was purchased (Invivogen, #tlrl-stfla). Designs were purified as described in Chapter 2.

Biolayer interferometry

BLI was performed on an Octet RED96 or Octet R8. All biosensors were hydrated in kinetics buffer HBS-EP+ (10 mM HEPES, 150 mM NaCl, 3 mM EDTA, 0.05% v/v surfactant P20) with 0.5% w/v non-fat dry milk (Cytiva). Flagellin was biotinylated and excess biotin was purified out by SEC. Biotinylated flagellin was diluted to a final concentration of 0.01 mg/mL in kinetics buffer and loaded onto streptavidin biosensors (Sartorius). TLR5-FC was diluted in kinetics buffer to 500 nM and its association was measured for 300 s, followed by a dissociation for 300 s in kinetics buffer.

Negative Stain Electron Microscopy

400-mesh carbon coated grids (Electron Microscopy Sciences) were glow-discharged and 3 uL of TLR-FC at 20 ug/mL was applied and then stained with 2% (w/v) uranyl formate. All nsEM data were collected with a BM-Ceta camera at 57,000x magnification using EPU 2.0 on a 120 kV Talos L120C transmission electron microscope (Thermo Scientific). CTF processing, particle picking, particle extraction, 2D classification, and 3D refinement steps were all performed with CryoSPARC[93].

HEK-Blue™ and Ramos-Blue™ activation assays

Cells were cultured as described in the manufacturer’s technical data sheet (InvivoGen).

NanoDSF

All proteins were formulated at 0.2 mg/mL in 25 mM Tris, pH 8.0, 150 mM NaCl and then mixed at 9 volumes to 1 volume of 200× concentrate SYPRO orange (Thermo Fisher) diluted in the same buffer. NanoDSF to determine melting temperatures was carried out on an UNcle (UNchained Labs) by measuring the integration of fluorescence emission spectrum during a thermal ramp from 25°C to 95°C, with a 1°C increase in temperature per minute.

Endotoxin Removal and Testing

Endotoxin was removed from samples by including 0.75% CHAPS in the lysis buffer and performing multiple 0.75% CHAPS + PBS washes before eluting the samples off of Nickel. SEC columns were thoroughly cleaned before purification and endotoxin levels were measured using the EndoSafe Nexgen-MCS system (Charles River). Samples were diluted in endotoxin-free water and applied to EndoSafe LAL reagent cartridges.

Immunogenicity Studies

For immunogenicity studies, mice were housed in a specific-pathogen free facility within the Department of Comparative Medicine at the University of Washington, Seattle, accredited by the Association for Assessment and Accreditation of Laboratory Animal Care (AAALAC). Animal studies were conducted in accordance with the University of Washington's Institutional Animal Care and Use Committee. Whole blood was collected in serum separator tubes (BD #365967) and rested for 30 min at room temperature for coagulation. Tubes were then centrifuged for 10 min at 2,000 *g* and serum was collected and stored at –80°C until use.

Enzyme-linked immunosorbent assay (ELISA)

Costar 96-well high protein binding plates were coated overnight at 4°C with HexaPro at and blocked in 200 uL of blocking buffer composed of (TBST: 1x Tris-buffered saline with 25 mM Tris pH 8.0, 150 mM NaCl, 0.2% Tween 20, and 5% nonfat milk). Plates were then washed 3x with TBST in an automated plate washer (Biotek); all washing steps follow the same protocol. Serum dilutions were plated and incubated for one hour at room temperature shaking at 500 rpm. Plates were washed before 100 uL per well of TMB were added and developed for 3 minutes, then quenched with 100 uL of 1N HCl. Reading at absorbance at 450 nM was carried out with an Epoch plate reader (Biotek).

Table 1: Amino Acid Sequences

Idealized Designs	Amino Acid Sequence

NJ10	DEEVEEWARRFFEWVRIALERASAESSEIESVWKELEQRARELLEELEKVLKTSTDEDEEDARAEALFRLALFMLNVVQRMRELAVQVANTAPFDYTDFKEAAERAVEWADTLRSRALAEKNRAESEKTN
NJ24	DEEEAERLVKEADKVRSEVLRWLNRLRSQATNENREVREESEEAERKLKAALLWLNVAQRIRELLVQVKERNATDSVKEEIEQREEELRRIREKT
NJ28	DEEAESVLKEIKQREEELEKAREELERTRSNDEREEMELRMRAALFALNVAQRARELLVQVDADRDEREEEKARKLVEWADEWRSRVARMLNRLESEQTN
NJ29	DEEADSVRKEIEQREEELKKLEEEARRTEADEEKKAKVLLELALKWLNVAQRIRELLVQVSAPTDKREEEKAEREVKKADELRSKVLRIMNRVKSEKTN
NJ32	SEEEAKKRLKEAEARLKAALWMFNVIQRMRELLVQVFNLVRRAGKDEARELLKSVNKELEQRARELMEWVENTEANDEKVKTIAEEIMKAVEEARNNNAEETAMKAMEKAVRLADELRSEALALLNRVRSLETN

MPNN Designs	**Amino Acid Sequence**
1	KFDINYNKELEEEKENLNKSQSSLSSAIERLSSGCRINSAKDDAAGQAIANRFTSNIKGLTQASRNANDGISIAQTTEGALNEINNNLQRVRELSVQATNGTNSDSDLKSIQDEIQQRLEEIDRVSNQTQFNGVKVLSQDNQMKIQVGANDGETITIDLQKIDVKSLGLDGFNVNGSGSTANPLASIDSALSKVDAVRSSLGAIQNRFDSAITNLGNTVTNLNSARSRIECADYATEVSNMSKAQILQQAGTEKLKEAEEKIEKYKELLKGGSGLNDIFEAQKIEWHE
2	NLNKSQSSLSSAIERLSSGCRINSAKDDAAGQAIANRFTSNIKGLTQASRNANDGISIAQTTEGALNEINNNLQRVRELSVQATNGTNSDSDLKSIQDEIQQRLEEIDRVSNQTQFNGVKVLSQDNQMKIQVGANDGETITIDLQKIDVKSLGLDGFNVNGSGSTANPLASIDSALSKVDAVRSSLGAIQNRFDSAITNLGNTVTNLNSARSRIECADYATEVSNMSKAQILQQAGTGGSGLNDIFEAQKIEWHE
3	AQDLSTNSLSLLTQNNLNKSQSSLSSAIERLSSGLRINSAKDDAAGQAIANRFTSNIKGLTQASRNANDGISIAQTTEGALNEINNNLQRVRELSVQATNGTNSDSDLKSIQDEIQQRLEEIDRVSNQTQFNGVKVLSQDNQMKIQVGANDGETITIDLQKIDVKSLGLDGFNVNGSGSTANPLASIDSALSKVDAVRSSLGAIQNRFDSAITNLGNTVTNLNSARSSIEDADYEQETQNMSKAQQ

NVQKGTTLQAQADQVPLNVLKQLLGGSGLNDIFEAQKIEWHE

4 AQVINTNSTSLLTQEELRKAQSSLSSAQERLSSGKRINSAKDDAAGQAI
ANRFTSNIKGLTQASRNANDGISIAETTEGALNEINNNLQRVKELSKQAT
NGTNSDSELKSIQDEIQQRLERIDEVSNQTQFNGVKVLSQDNQMKIQV
GANDGETITIDLQKIDVKSLGLDGFNVNGSGSTANPLASIDSALSKVDAV
RSSLGAIQNRFDSAITNLGNTVTNLNSERSLIEDADYETEVSNMEKAQK
EVQAGQSVLAQANQQPQNVLSLLRGGSGLNDIFEAQKIEWHE

5 AQVINTNSTSLLTQEELRKAQSSLSSAQERLSSGCRINSAKDDAAGQAI
ANRFTSNIKGLTQASRNANDGISIAETTEGALNEINNNLQRVKELSKQAT
NGTNSDSELKSIQDEIQQRLERIDEVSNQTQFNGVKVLSQDNQMKIQV
GANDGETITIDLQKIDVKSLGLDGFNVNGSGSTANPLASIDSALSKVDAV
RSSLGAIQNRFDSAITNLGNTVTNLNSERSLIECADYETEVSNMEKAQK
EVQAGQSVLAQANQQPQNVLSLLRGGSGLNDIFEAQKIEWHE

6 AQVINTNSTSLLTQNELNKAQSSLSSAQERLSSGKRINSAKDDAAGQAI
ANRFTSNIKGLTQASRNANDGISIAETTEGALNSINNNLQRVKELSKQAT
NGTNSDSELKSIQDEIQQRLERIDEVSNQTQFNGVKVLSQDNQMKIQV
GANDGETITIDLQKIDVKSLGLDGFNVNGSGSTANPLASIDSALSKVDAV
SSSLGAISNRFDSAITNLGNTVTNLNSERSLIEDADYETEVSNMEKAQK
EVQAGQSVLAQANQQPQNVLKELRGGSGLNDIFEAQKIEWHE

7 AQDLNFNSVSAETQKQLEKAQSSLSSAQERLKSGRRINSIKDDAAGLAI
ANRFTSEIKGLTQASRNANDGIAIAETTEGALDEINNNLQRVKELSVQAT
NGTNSDSDLKSIQDEIQQRLEEIDRVSNQTQYNGVKVLSQDNQMKIQV
GANDGETITIDLQKIDVKSLGLDGFNVNGSGSTANPLASIDSALSKVDAV
RSSLGAIQNRFDSAITNLGNTVTNLNSQRSSIEDADYQTEVSNMQKAQ
EEVQAGQSVLAQANQIPQNVLSLLRGGSGLNDIFEAQKIEWHE

8 AQDLNFNSVSAETQKQLEKAQSSLSSAQERLKSGCRINSIKDDAAGLAI
ANRFTSEIKGLTQASRNANDGIAIAETTEGALDEINNNLQRVKELSVQAT
NGTNSDSDLKSIQDEIQQRLEEIDRVSNQTQYNGVKVLSQDNQMKIQV
GANDGETITIDLQKIDVKSLGLDGFNVNGSGSTANPLASIDSALSKVDAV
RSSLGAIQNRFDSAITNLGNTVTNLNSQRSSIECADYQTEVSNMQKAQ
EEVQAGQSVLAQANQIPQNVLSLLRGGSGLNDIFEAQKIEWHE

9 AQDLSFNSLSQLTQNELQKAQSSLSSAQERLKSGRRINSVKDDAAGLAI
ANRFTSNIKGLTQASRNANDGIDIARTTEGALDEINNNLQRVKELSLQAT
NGTNTDSQLKSIQDEIQQRLEHIDKVSNQTQYNGVKVLSQDNQMKIQV
GANDGETITIDLQKIDVKSLGLDGFNVNGSGSTANPLASIDSALSKVDAV
RSSLGAIQNRFDSAITNLGNTVTNLNSARSRIEDADYETEVSNMQKAQQ
LVQAGQSVLAQANQVPQNVLSLLRGGSGLNDIFEAQKIEWHE

10 AQDLSFNSLSQLTQNELQKAQSSLSSAQERLKSGCRINSVKDDAAGLAI
ANRFTSNIKGLTQASRNANDGIDIARTTEGALDEINNNLQRVKELSLQAT
NGTNTDSQLKSIQDEIQQRLEHIDKVSNQTQYNGVKVLSQDNQMKIQV
GANDGETITIDLQKIDVKSLGLDGFNVNGSGSTANPLASIDSALSKVDAV
RSSLGAIQNRFDSAITNLGNTVTNLNSARSRIECADYETEVSNMQKAQQ
LVQAGQSVLAQANQVPQNVLSLLRGGSGLNDIFEAQKIEWHE

11 AQDLSHNSVSEETENELKKAQSSLSSAQERLKSGKRINSVKDDAAGLAI
ANRFTSEIKGLTQASRNANDGISIARTTEGALDEINNNLQRVRELSVQAT
NGTNSDSELKSIQDEIQQRLENIDRVSNQTQFNGVKVLSQDNQMKIQV
GANDGETITIDLQKIDVKSLGLDGFNVNGSGSTANPLASIDSALSKVDAV
RSSLGAIQNRFDSAITNLGNTVTNLNSQRSKIEDADYATEVSNMSKAQIL
VQAGKSVLAQAKQIPQNVLSLFRGGSGLNDIFEAQKIEWHE

12 AQDLSHNSVSEETENELKKAQSSLSSAQERLKSGCRINSVKDDAAGLAI
ANRFTSEIKGLTQASRNANDGISIARTTEGALDEINNNLQRVRELSVQAT
NGTNSDSELKSIQDEIQQRLENIDRVSNQTQFNGVKVLSQDNQMKIQV
GANDGETITIDLQKIDVKSLGLDGFNVNGSGSTANPLASIDSALSKVDAV
RSSLGAIQNRFDSAITNLGNTVTNLNSQRSKIECADYATEVSNMSKAQIL
VQAGKSVLAQAKQIPQNVLSLFRGGSGLNDIFEAQKIEWHE

13 RINHNIAALNTRNRLGSNNGAAQKNMEKLSSGLRINRAGDDAAGLAES
EKMRGEIRGLEQASKNSQDGISLIQTAEGALTTTHAILQRMRELTVQAG
NTGTQQEEELGAIKDEMDALIEEIDGISNRTEFNGKKLLDGTNSTDGFTF
QIGAEAGQQLNVKIDSMSSTALGVNALDVTDFAATAFDDQLKSIDTAINT
VSTQIAKLGAVINRLEHTIQNLGASGENLTAAESKIRDVDMEKMKKEFDK
KNVETDKAKEDLKKANEIPINVLKKLEGGSGLNDIFEAQKIEWHE

14 RINHNIAALNTKNRLGSNNGAAQKNMEKLSSGLRINRAGDDAAGLALSE
KMRGLIRGLEQASKNSQDGISLIQTAEGALTRTHAILQRMRELTVQAGN
TGTQQEEELGAIKDEMDALIEEIDGISNRTEFNGKKLLDGTNSTDGFTFQ
IGALAGQQLNVKIDSMSSTALGVNALDVTDFAATAFDDQLKSIDTAINTVS
TQIAKLGAVINRLEHTISNLGASGENLTAAESSIRDVDMEKMREEFDKNN
KLTEQAEKDLKKANEIPINELKKLEGGSGLNDIFEAQKIEWHE

15 RINHNIAALNTKNRLGSNNGAAQKNMEKLSSGLRINRAGDDAAGLALSE
KMRGTIRGLEQASKNSQDGIKLIQTAEGALTRTHAILQRMRELTVQAGN
TGTQQEEELGAIKDEMDALIEEIDGISNRTEFNGKKLLDGTNSTDGFTFQ
IGAEAGQQLNVKIDSMSSTALGVNALDVTDFAATAFDDQLKSIDTAINTV
STQIAKLGAVINRLEHTISNLGASGENLTAAESSIRDVDMEKMKEEFDKN
NKLTLDSQKELENANLVPINQLNLLEGGSGLNDIFEAQKIEWHE

16 RINHNIAALNTRNRLGSNNGAAQKNMEKLSSGCRINRAGDDAAGLAES

EKMRGEIRGLEQASKNSQDGISLIQTAEGALTTTHAILQRMRELTVQAG
NTGTQQEEELGAIKDEMDALIEEIDGISNRTEFNGKKLLDGTNSTDGFTF
QIGAEAGQQLNVKIDSMSSTALGVNALDVTDFAATAFDDQLKSIDTAINT
VSTQIAKLGAVINRLEHTIQNLGASGENLTAAESKIRCVDMEKMKKEFDK
KNVETDKAKEDLKKANEIPINVLKKLEGGSGLNDIFEAQKIEWHE

17 RINHNIAALNTKNRLGSNNGAAQKNMEKLSSGCRINRAGDDAAGLALS
EKMRGLIRGLEQASKNSQDGISLIQTAEGALTRTHAILQRMRELTVQAG
NTGTQQEEELGAIKDEMDALIEEIDGISNRTEFNGKKLLDGTNSTDGFTF
QIGALAGQQLNVKIDSMSSTALGVNALDVTDFAATAFDDQLKSIDTAINT
VSTQIAKLGAVINRLEHTISNLGASGENLTAAESSIRCVDMEKMREEFDK
NNKLTEQAEKDLKKANEIPINELKKLEGGSGLNDIFEAQKIEWHE

18 RINHNIAALNTKNRLGSNNGAAQKNMEKLSSGCRINRAGDDAAGLALS
EKMRGTIRGLEQASKNSQDGIKLIQTAEGALTRTHAILQRMRELTVQAG
NTGTQQEEELGAIKDEMDALIEEIDGISNRTEFNGKKLLDGTNSTDGFTF
QIGAEAGQQLNVKIDSMSSTALGVNALDVTDFAATAFDDQLKSIDTAINT
VSTQIAKLGAVINRLEHTISNLGASGENLTAAESSIRCVDMEKMKEEFDK
NNKLTLDSQKELENANLVPINQLNLLEGGSGLNDIFEAQKIEWHE

19 RLNHNKLAEELEKRLGSSNGAAQRNKEKLSSGLRINRAGDDAAGLELS
EKMRGRIRGLEEASKNSQDGIKLIQTAEGALTETHAILQRMKELTVQAG
NTGTQQPEQLGAIKDEMDALIEEIDGISNRTKFNGKKLLDGTNSTDGFT
FQIGAEAGDQLNVKIDSMSSTALGVNALDVTDFAATAFDDQLKSIDTAIN
TVSTQQAKLGAVINRLEHTIKNLGASGENLTAAESSIMDVDMAKVQSELT
KENILTKAAEAMLKEAKKVPLNVLKLLEGGSGLNDIFEAQKIEWHE

20 RLNHNKLAEELEKRLGSSNGAAQRNKEKLSSGCRINRAGDDAAGLELS
EKMRGRIRGLEEASKNSQDGIKLIQTAEGALTETHAILQRMKELTVQAG
NTGTQQPEQLGAIKDEMDALIEEIDGISNRTKFNGKKLLDGTNSTDGFT
FQIGAEAGDQLNVKIDSMSSTALGVNALDVTDFAATAFDDQLKSIDTAIN
TVSTQQAKLGAVINRLEHTIKNLGASGENLTAAESSIMCVDMAKVQSELT
KENILTKAAEAMLKEAKKVPLNVLKLLEGGSGLNDIFEAQKIEWHE

21 RLNHNIKALNLQNRLGSANGAAQKNEEKLSSGLRINRAGDDAAGLALS
EKMRGLIRGLEEASKNSQDGISLIQTAEGALTETHAILQRMKELTVQAGN
TGTQQPEQLGAIKDEMDALIERIDGISNRTTFNGKKLLDGTNSTDGFTF
QIGAEAGQQLNVKIDSMSSTALGVNALDVTDFAATAFDDQLKSIDTAINT
VSTQQAKLGAVINRLEHTIRNLGASGENLTAAESKIQDVDMEKVQEELD
KQNEEIKQAQKELEEAQKEPLNLLELLKGGSGLNDIFEAQKIEWHE

22 RLNHNIKALNLQNRLGSANGAAQKNEEKLSSGCRINRAGDDAAGLALS
EKMRGLIRGLEEASKNSQDGISLIQTAEGALTETHAILQRMKELTVQAGN

	TGTQQPEQLGAIKDEMDALIERIDGISNRTTFNGKKLLDGTNSTDGFTFQIGAEAGQQLNVKIDSMSSTALGVNALDVTDFAATAFDDQLKSIDTAINTVSTQQAKLGAVINRLEHTIRNLGASGENLTAAESKIQCVDMEKVQEELDKQNEEIKQAQKELEEAQKEPLNLLELLKGGSGLNDIFEAQKIEWHE
23	RINHNEEAEKLLERLGSRNGAAQQNMEKLSSGLRINRAGDDAAGLAESEKMRGLIRGLEEASKNSQDGIELIQTAEGALTETHAILQRMRELTVQAGNTGTQQPEELGAIKDEMDALIERIDGISNRTTFNGKKLLDGTNSTDGFTFQIGAEAGEQLNVKIDSMSSTALGVNALDVTDFAATAFDDQLKSIDTAINTVSTQMAKLGAVMNRLEHTIENLGASGENLTAAESKINDVDMEKVKEELNKENEEIEEAKKELEKAKEKPKNLLKKLKGGSGLNDIFEAQKIEWHE
24	RINHNEEAEKLLERLGSRNGAAQQNMEKLSSGCRINRAGDDAAGLAESEKMRGLIRGLEEASKNSQDGIELIQTAEGALTETHAILQRMRELTVQAGNTGTQQPEELGAIKDEMDALIERIDGISNRTTFNGKKLLDGTNSTDGFTFQIGAEAGEQLNVKIDSMSSTALGVNALDVTDFAATAFDDQLKSIDTAINTVSTQMAKLGAVMNRLEHTIENLGASGENLTAAESKINCVDMEKVKEELNKENEEIEEAKKELEKAKEKPKNLLKKLKGGSGLNDIFEAQKIEWHE

Chapter 4. De novo design of TREM-2 minibinders

Abstract

TREM-2 is an important receptor whose inhibition can lead to therapeutic effects in neurodegeneration and cancer. Here, we describe the design of minibinders to inhibit TREM-2. Computational design yielded positive results, but experimental testing was inconclusive.

Introduction

We encountered several challenges when designing binders for Toll-like Receptors. These challenges included difficulties in obtaining recombinant ectodomain (Chapter 3-TLR5) and activating endosomal receptors (Chapter 2-TLR3). We strived to find a target that was natively expressed on the cell surface and had an exposed hydrophobic patch away from a glycan. Additionally, the target needed a high-resolution structure of the human ectodomain.

I began scouring the literature for other innate immune receptors that might fit this criteria. This led me to the TREM (Triggering receptor expressed on myeloid cells) family, a class of innate immune receptors that can amplify or inhibit TLR signaling[118]. TREM-1 synergizes with the TLR pathway[119]. Attempting activation of this target seemed like it would result in some of the same issues as the TLRs (can we induce non-native activation via non-specific receptor clustering). TREM-2, however, inhibits TLR signaling[120]. Perhaps inhibiting an inhibitor could lead to increased TLR signaling.

Outside of a vaccine context, TREM-2 has been linked to neurodegenerative diseases and has been shown to play a role in the tumor microenvironment[121,122]. A landmark study showed that using antibodies to inhibit TREM-2 decreases certain tumor growth[123]. Furthermore, inhibiting both TREM-2 and programmed death-1 (PD-1) leads to enhanced anti-PD-1 immunotherapy[123]. This was particularly interesting because it showed inhibition of a receptor rather than activation could lead to a biological response. Our goal here was to create TREM-2 binders to inhibit TREM-2 signaling.

Results

Computational design of TREM-2 minibinders

TREM-2 has one glycan on N79 (**Fig.1a**). We selected a hydrophobic patch away from the glycan for minibinder design (**Fig.1b**). The RifDock pipeline[47] was used to design minibinders as described in the TLR3 chapter. Trp44, Asn68, Leu69, Trp70, Leu71, Leu72, Phe74, Leu75, and Leu89 were used as the core hydrophobic patch for PatchDock. The residues for RifGen included PatchDock residues and additional residues: Met41, Gly45, Arg46, His67, Ser73, Arg77, Thr88. The starting scaffolds were 3 helical miniproteins. We selected 15,000 designs for yeast surface display.

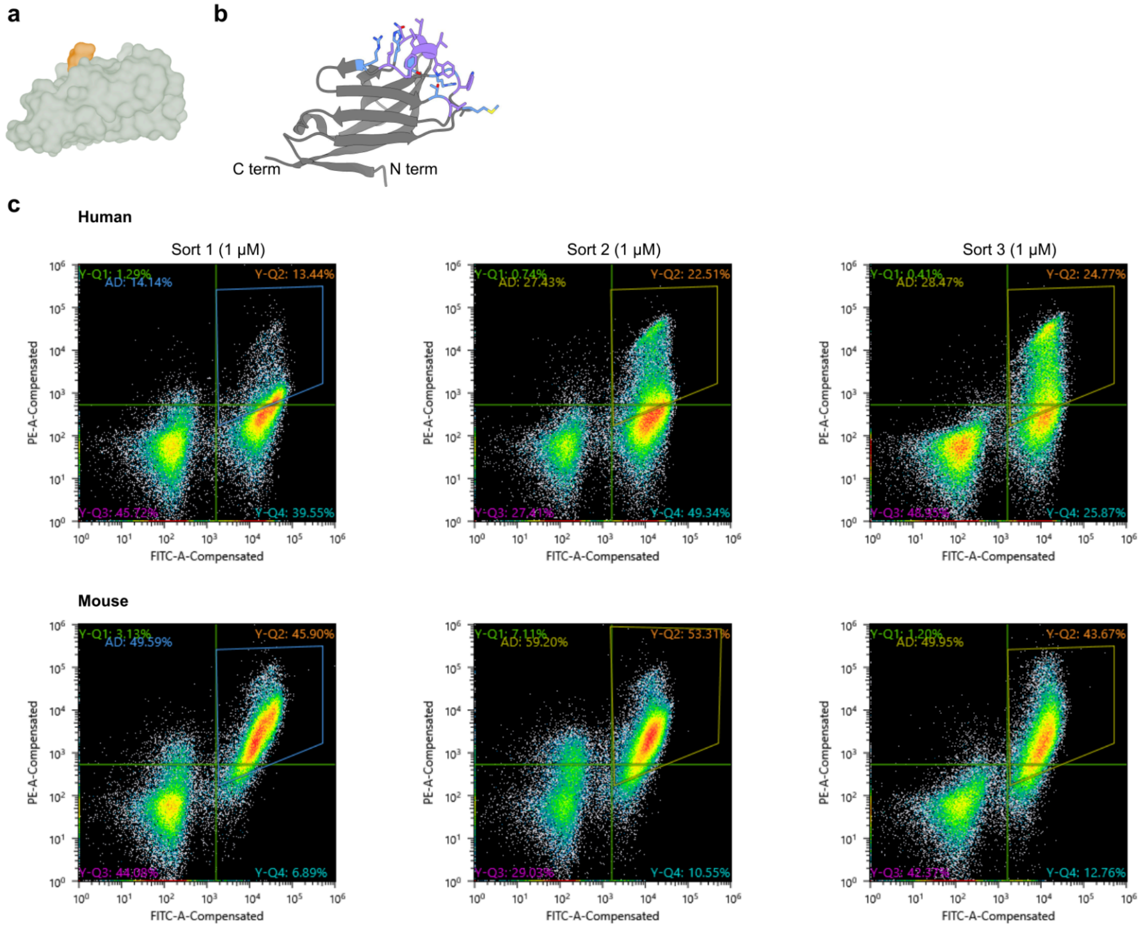

Fig. 1. Design and screening of TREM-2 minibinders.
a, Surface representation of TREM-2. The N79 Glycan is labeled in brown. **b,** The RifDock pipeline was used to design *de novo* miniproteins. Purple residues were used in PatchDock and RifGen. Blue residues were used in RifGen. **c,** 15,000 designs were tested using yeast surface display against human and mouse ectodomain.

Biochemical characterization of TREM-2 minibinders

Yeast surface display was performed as described in the TLR3 chapter (**Fig. 1c**). The library was sorted for expression (FITC+). Then, the library was sorted in parallel against human and mouse receptors. In the first sort, 12.35% and 46.28% of cells appeared in the top right quadrant respectively. This is a much higher percentage than expected in the first sort. Subsequent sorts continued to show a high percentage.

To identify if the TREM-2 receptor was non-specific, I sorted the TLR3 binder library against mouse TREM-2, resulting in an 8% binding population. The TLR3 binder library against human TREM-2 showed a 1.74% binding population. Notably, the TLR3 binder library showed 0.55% binding against the TLR2 receptor. This suggests there was some degree of non-specificity with the TREM-2 receptor.

Discussion

This project remains incomplete at the conclusion of the PhD. While computational design against TREM-2 led to a library of 15,000 promising binders *in silico*, initial yeast screening showed that the TREM-2 recombinant protein was sticking nonspecifically to binders. Given the large hydrophobic patch on TREM-2, this was not surprising.

If this study were to be repeated, several changes may increase the chances of success. Increasing the percent of BSA in the sorting buffer may help with non-specificity. Targeting a different site on TREM-2 would allow for the hydrophobic mutations in TREM-2 to be mutated or obscured by a bound antibody. A different scaffold library would allow for more sites on TREM-2 to be targeted. As computational methods develop, binder success rate also improves. Screening a smaller library of binders with a different binding method, e.g., BLI or SPR, would be useful.

Although this project is left in an incomplete state, important lessons can be derived from this work. It is important to be practical when choosing your target receptor and screening methods.

Acknowledgements

Thank you to Inna Goreshnik, Aza Allen, Cami Cordray, Samer Halabiya, and Dionne Vafeados for help with yeast library preparation.

Materials and Methods

Computational Design

The ectodomain of TREM-2 (PDB 5ELI) was used for design. Methods are as described in Chapter 2 of this work.

Library preparation

Library preparation is described in Chapter 2 of this work.

Yeast Surface Display.

Yeast display is described in Chapter 2 of this work. Sorts 1 and 2 were tested with avidity. Sort 3 was tested without avidity.

Protein expression and purification

Biotinylated and FC-fused TREM-2 was purchased from Acro Biosystems.

Chapter 5. De novo design of FcγRIIA/B minibinders

Abstract

FcγRIIA is an important receptor whose activation can lead to the opsonization of pathogens and the production of CD8+ T cells. Here, we describe the design of minibinders to activate FcγRIIA. Computational design yielded positive results, but experimental testing demonstrated binders were cross reactive to FcγRIIB.

Introduction

CD8+ T cells can kill infected cells and are an important part of an effective vaccine response. Subunit vaccines require adjuvants to elicit strong CD8+ responses[124]. Work in the field has shown that targeting the FC gamma receptors (FcγRs) can lead to an increased CD8+ response, maturation of dendritic cells, and overall survival in a flu therapy model[125]. This makes FcγRs a promising adjuvant target.

The FcγRs are a subclass of Fc receptors that bind to and are activated by the Fc portion of IgGs[126]. FcγRs have a low affinity to IgGs alone, but when IgGs form immune complexes around a pathogen, FcγRs are activated and can phagocytize the pathogen[127-128]. There are three classes of FcγRs in humans: FcγRI, FcγRIIA/B, FcγRIIIA/B[129]. All of these are activating receptors, except for RIIB. These classes are expressed on different leukocytes and have varying affinities for different IgG subtypes[130]. Modifying antibodies to selectively target FcγRIIA over FcγRIIB (highly similar in sequence) led to an increased CD8+ response[125].

Here we describe the design of minibinders against FcγRIIA in hopes of creating a potent binder that can be multivalently displayed on a nanoparticle and subsequently activate FcγRIIA.

Results

Computational design of minibinders

We selected a patch of residues on the C-term side of the FcγRIIA (on the immunoglobulin domain furthest from the membrane) (**Fig. 1a**). We purposefully stayed away from sites where there are naturally occurring alleles and glycans. However, at the time of design we were ignorant of how similar FcγRIIB was to FcγRIIA at this site (near identical).

We used the Rosetta RifDock pipeline[47] to design a library of candidate minibinders (as described in Chapter 2). We cloned synthetic oligonucleotides encoding the designs into an expression vector to enable screening by yeast surface display[55] and used fluorescence-activated cell sorting (FACS) to identify cells expressing miniproteins that bound fluorescently labeled FcγRIIA. After two rounds of sorting with 1 μM streptavidin-tetramerized FcγRIIA as a probe, we observed a clear population of double-positive cells (**Fig. 1b**).

Enrichment of this population by subsequent sorts without avidity (i.e., with monomeric FcγRIIA) resulted in high numbers of FcγRIIA-binding cells at 50 nM of receptor that decreased to near-background levels at 10 nM. Sequencing double-positive cells from each sort identified 8 hits out of 21,829 candidates, a success rate consistent with previous applications of this methodology[47]. An example hit is shown (**Fig.1c**)

Screening functionality

Four minibinders were biotinylated and bound to neutravidin beads at varying ratios. Splenic B cells and peritoneal cavity macrophages were isolated from mice that had human RIIA knocked in (KI) or knocked out (KO). The beads were then incubated with the primary cells and the percent bound was reported (**Fig. 2a**). Minibinders 1, 3, and 5 showed clear dose-dependent binding in B cells derived from KI mice. All minibinders bound to macrophages derived from KI mice (**Fig. 2c**).

B1gp45 is a protein that binds *Acinetobacter baumannii*. B1gp45 was linked to minibinder 5 and bacterial clearance was measured *in vitro* and *in vivo*. Minibinder 5 linked to B1gp45 promoted clearance of *A. baumanni* over B1gp45 alone in FcγRII KI mice.

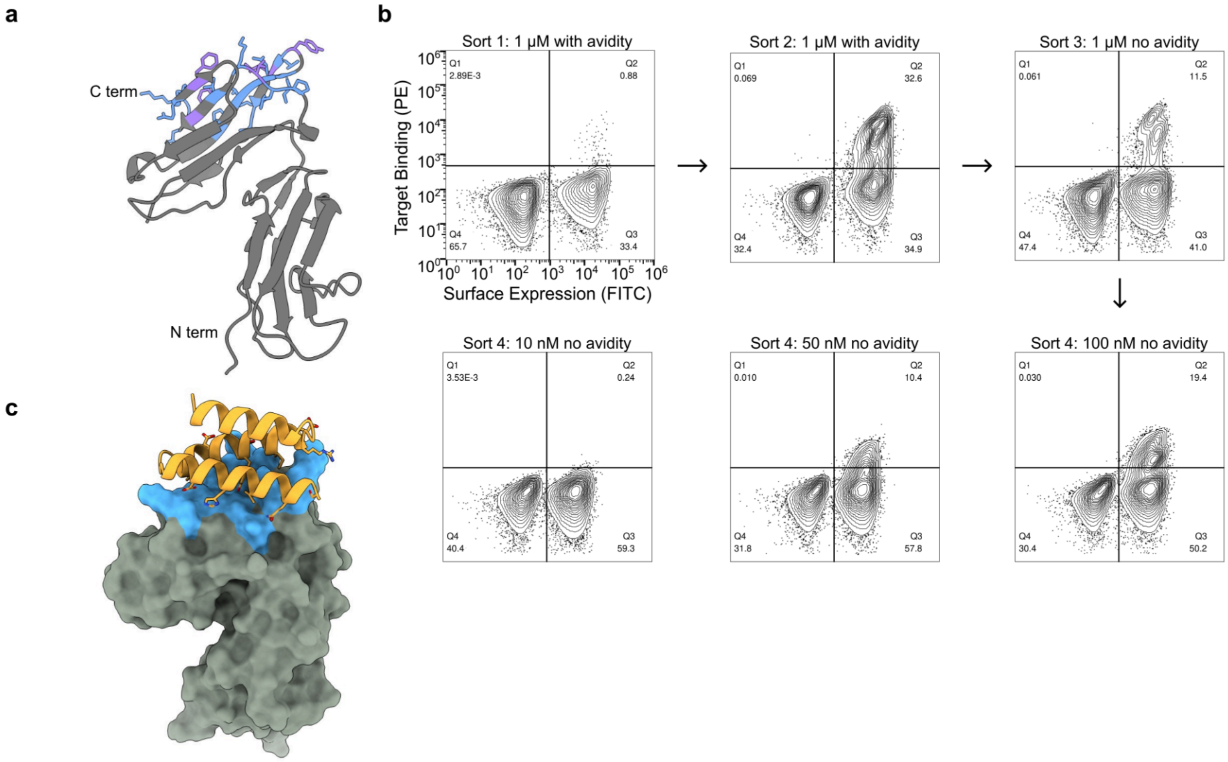

Fig. 1. Design of RIIA binders

a, The RifDock pipeline was used to design *de novo* miniproteins. Purple residues were used in PatchDock and RifGen. Blue residues were used in RifGen. **b,** 21,829 designs were tested using yeast surface display against decreasing concentrations of FcγRIIA. **c,** Model of minibinder 5 bound to FcγRIIA.

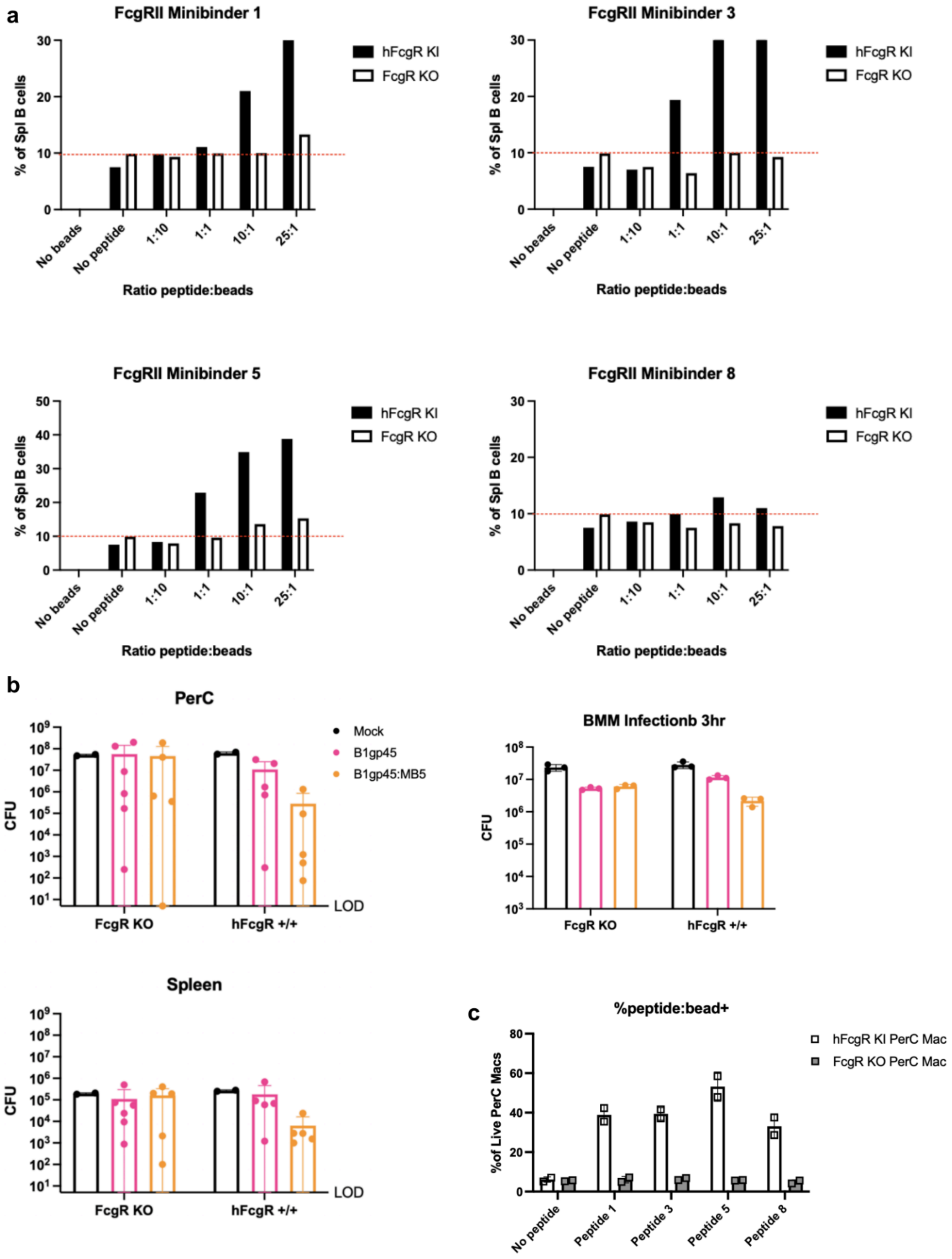
a
FcgRII Minibinder 1
FcgRII Minibinder 3
FcgRII Minibinder 5
FcgRII Minibinder 8
% of Spl B cells
hFcgR KI
FcgR KO
No beads
No peptide
1:10
1:1
10:1
25:1
Ratio peptide:beads
0
10
20
30
40
50
b
PerC
Spleen
BMM Infectionb 3hr
CFU
Mock
B1gp45
B1gp45:MB5
FcgR KO
hFcgR +/+
LOD
10^1
10^2
10^3
10^4
10^5
10^6
10^7
10^8
10^9
c
%peptide:bead+
%of Live PerC Macs
hFcgR KI PerC Mac
FcgR KO PerC Mac
No peptide
Peptide 1
Peptide 3
Peptide 5
Peptide 8
0
20
40
60
80

Fig. 2. Activity of minibinders.
a, Four different minibinders on fluorescent beads were tested for binding against B cells isolated from Knock In (KI) and Knock Out (KO) Fcγ humanized mice. **b,** Clearance of *A. baumannii* by macrophages with addition of minibinder 5/B1gp45 beads *in vivo* 8 hours post infection in the peritoneal cavity or spleen or *in vitro* tissue culture. **c,** Four different minibinders were tested for binding against macrophages isolated from Knock In (KI) and Knock Out (KO) Fcγ humanized mice.

Discussion

The goal of this project was to create minibinders that could bind to and activate RIIA. We clearly showed that the designed binders can bind to FcγRIIA via yeast display, BLI, *in vitro* and *in vivo* experiments. Unfortunately, the design was done without the knowledge that FcγRIIB, the inhibitory receptor, is nearly identical to RIIA at the chosen site. The minibinders do bind to FcγRIIB, as expected. Though cross-reactive, the minibinders still appear to have an effect *in vitro*.

At this point in the project, the project was handed off to an incoming graduate student, Charlie Clarke. He initiated a new design campaign to target sites that differ between FcγRIIA and FcγRIIB, though it is difficult to find such a site[131]. The initial efforts outlined here have guided our future design. New methods, such as RFDiffusion[83] could be used to graft known FcγRIIA-selective antibody binding loops[132] onto minibinders.

Acknowledgements

Thank you to Jake Kraft for the initial idea. Thank you Charlie Clarke for helping test and characterize designs. Thank you to Dr. Lieselotte Kreuk of the Woodward Lab for doing all of the mouse experiments.

Materials and Methods

Computational design

To try to increase the success rate of designs, two different approaches were tried. The first was to do design as normal (as described in TLR3 section). The second was to include a flag that counted all polar patchdock residues as hydrophobic. This was done with the flag “-count_all_contacts_as_hydrophobic”. This artificially increases the contact patch scores. Ultimately, they led to a similar amount of designs that passed other filtering metrics.

Yeast Surface Display

Designs were first sorted for expression using FITC+ cells as a metric for expression. All sorts were performed using FcγRIIA R167 (as opposed to FcγRIIA H167). The first two sorts were performed at 1 μM of receptor with avidity. Sort 3-4 were done with no avidity with decreasing concentrations of FcγRIIA. Robust double positive cells, indicating binding, were seen at Sorts 2-4. Cells were collected after each sort and submitted for NGS sequencing.

In vitro data

Bone marrow derived macrophages (BMM) were infected with *A. baum* +/- B1gp45:minibinder 5. After 3 hours, colony forming units in cells were determined. B1gp45 and minibinder 5 were linked with the LHD fusion system[133].

In vivo data

Intraperitoneal (IP) infection with *A. baum*. Protein was injected IP 1 hour after infection. Mice were sacrificed at 8 hours post infection.

Chapter 6. Conclusions

In this dissertation, we explored the design and stabilization of novel protein binders targeted at various immune receptors including TLR3, TLR5, FcγRIIA, and TREM-2.

Our investigations into TLR3 minibinders demonstrated their potential as novel adjuvants to enhance immune responses. These binders were designed to specifically activate the TLR3 pathway, showing promising results *in vitro* through the induction of NF-κB signaling pathways. TLR3's native ligand is dsRNA, so this is great progress towards a protein adjuvant, but the transition from *in vitro* to *in vivo* will not be trivial.

In the case of TLR5, our efforts to stabilize flagellin variants were successful *in vitro*, but again there were challenges when translating to *in vivo*. The flagellin-based designs did not produce the expected enhancement in immunogenic response when paired with the RBD antigen, suggesting that the choice of antigen can dramatically influence the outcome of adjuvant-based strategies. Notably, native flagellin did not also elicit an immune response.

The exploration of minibinders targeting FcγRIIA and TREM-2 revealed insights into how specificity and cross-reactivity in receptor families matter. While computational design can be straightforward, biology is not.

In sum, this work summarizes the application of established protein design pipelines to four different targets. As protein design continues to advance, binder design will become trivial. Understanding receptor biology is crucial to advancing towards protein based adjuvants. It is my hope that the lessons learned here are useful to future designers.

References

1. Pollard, A. J. & Bijker, E. M. A guide to vaccinology: from basic principles to new developments. *Nat. Rev. Immunol.* **21**, 83–100 (2020).
2. Smith, K. A. Louis Pasteur, the Father of Immunology? *Front. Immunol.* **3**, (2012).
3. Dunn, G., Begg, N. T., Cammack, N. & Minor, P. D. Virus excretion and mutation by infants following primary vaccination with live oral poliovaccine from two sources. *J. Med. Virol.* **32**, (1990).
4. New generation adjuvants – From empiricism to rational design. *Vaccine* **33**, B14–B20 (2015).
5. HogenEsch, H. Mechanism of Immunopotentiation and Safety of Aluminum Adjuvants. *Front. Immunol.* **3**, (2012).
6. Taro Kawai, S. A. Pathogen recognition with Toll-like receptors. *Curr. Opin. Immunol.* **17**, 338–344 (2005).
7. Medzhitov, R., Preston-Hurlburt, P. & Janeway, C. A. A human homologue of the Drosophila Toll protein signals activation of adaptive immunity. *Nature* **388**, 394–397 (1997).
8. Akira, S., Takeda, K. & Kaisho, T. Toll-like receptors: critical proteins linking innate and acquired immunity. *Nat. Immunol.* **2**, 675–680 (2001).
9. Kim, H. M. *et al.* Crystal Structure of the TLR4-MD-2 Complex with Bound Endotoxin Antagonist Eritoran. *Cell* **130**, 906–917 (2007).
10. Bell, J. K. *et al.* The molecular structure of the Toll-like receptor 3 ligand-binding domain. *Proc. Natl. Acad. Sci. U. S. A.* **102**, 10976–10980 (2005).
11. Choe, J., Kelker, M. S. & Wilson, I. A. Crystal structure of human toll-like receptor 3 (TLR3) ectodomain. *Science* **309**, 581–585 (2005).
12. Sakaniwa, K. *et al.* TLR3 forms a laterally aligned multimeric complex along double-stranded RNA for efficient signal transduction. *Nat. Commun.* **14**, 164 (2023).
13. Jin, M. S. *et al.* Crystal structure of the TLR1-TLR2 heterodimer induced by binding of a tri-acylated lipopeptide. *Cell* **130**, 1071–1082 (2007).
14. Yoon, S.-I. *et al.* Structural basis of TLR5-flagellin recognition and signaling. *Science* **335**, 859 (2012).
15. Park, B. S. *et al.* The structural basis of lipopolysaccharide recognition by the TLR4-MD-2 complex. *Nature* **458**, 1191–1195 (2009).
16. Lim, C. S. *et al.* TLR3 forms a highly organized cluster when bound to a poly(I:C) RNA ligand. *Nat. Commun.* **13**, 6876 (2022).
17. Luo, J. *et al.* Lateral Clustering of TLR3:dsRNA Signaling Units Revealed by TLR3ecd:3Fabs Quaternary Structure. *J. Mol. Biol.* **421**, 112–124 (2012).
18. Akira, S. & Takeda, K. Toll-like receptor signalling. *Nat. Rev. Immunol.* **4**, 499–511 (2004).
19. O’Neill, L. A. J. & Bowie, A. G. The family of five: TIR-domain-containing adaptors in Toll-like receptor signalling. *Nat. Rev. Immunol.* **7**, 353–364 (2007).
20. Kawai, T. & Akira, S. Signaling to NF-kappaB by Toll-like receptors. *Trends Mol. Med.* **13**, 460–469 (2007).
21. Alexopoulou, L., Holt, A. C., Medzhitov, R. & Flavell, R. A. Recognition of

double-stranded RNA and activation of NF-kappaB by Toll-like receptor 3. *Nature* **413**, (2001).
22. Stetson, D. B. & Medzhitov, R. Type I interferons in host defense. *Immunity* **25**, 373–381 (2006).
23. Steinman, R. M. & Cohn, Z. A. Identification of a novel cell type in peripheral lymphoid organs of mice. I. Morphology, quantitation, tissue distribution. *J. Exp. Med.* **137**, 1142–1162 (1973).
24. Janeway, C. A., Jr. Approaching the asymptote? Evolution and revolution in immunology. *Cold Spring Harb. Symp. Quant. Biol.* **54 Pt 1**, 1–13 (1989).
25. Zhao, T. *et al.* Vaccine adjuvants: mechanisms and platforms. *Signal Transduct Target Ther* **8**, 283 (2023).
26. Duthie, M. S., Windish, H. P., Fox, C. B. & Reed, S. G. Use of defined TLR ligands as adjuvants within human vaccines. *Immunol. Rev.* **239**, 178–196 (2011).
27. Verma, S. K. *et al.* New-age vaccine adjuvants, their development, and future perspective. *Front. Immunol.* **14**, 1043109 (2023).
28. Didierlaurent, A. M. *et al.* AS04, an aluminum salt- and TLR4 agonist-based adjuvant system, induces a transient localized innate immune response leading to enhanced adaptive immunity. *J. Immunol.* **183**, 6186–6197 (2009).
29. Thoelen, S., De Clercq, N. & Tornieporth, N. A prophylactic hepatitis B vaccine with a novel adjuvant system. *Vaccine* **19**, 2400–2403 (2001).
30. CpG 7909: PF 3512676, PF-3512676. *Drugs R. D.* **7**, 312–316 (2006).
31. Brito, L. A., Malyala, P. & O'Hagan, D. T. Vaccine adjuvant formulations: a pharmaceutical perspective. *Semin. Immunol.* **25**, 130–145 (2013).
32. Pérez, O. *et al.* Human prophylactic vaccine adjuvants and their determinant role in new vaccine formulations. *Braz. J. Med. Biol. Res.* **45**, 681–692 (2012).
33. Muzio, M. *et al.* Differential expression and regulation of toll-like receptors (TLR) in human leukocytes: selective expression of TLR3 in dendritic cells. *J. Immunol.* **164**, 5998–6004 (2000).
34. Heinz, S. *et al.* Species-specific Regulation of Toll-like Receptor 3 Genes in Men and Mice*. *J. Biol. Chem.* **278**, 21502–21509 (2003).
35. Schmidt, K. N. *et al.* APC-independent activation of NK cells by the Toll-like receptor 3 agonist double-stranded RNA. *J. Immunol.* **172**, 138–143 (2004).
36. Cario, E. & Podolsky, D. K. Differential alteration in intestinal epithelial cell expression of toll-like receptor 3 (TLR3) and TLR4 in inflammatory bowel disease. *Infect. Immun.* **68**, 7010–7017 (2000).
37. Jiang, Z., Mak, T. W., Sen, G. & Li, X. Toll-like receptor 3-mediated activation of NF-κB and IRF3 diverges at Toll-IL-1 receptor domain-containing adapter inducing IFN-β. *Proceedings of the National Academy of Sciences* **101**, 3533–3538 (2004).
38. Longhi, M. P. *et al.* Dendritic cells require a systemic type I interferon response to mature and induce CD4+ Th1 immunity with poly IC as adjuvant. *J. Exp. Med.* **206**, 1589–1602 (2009).
39. Schulz, O. *et al.* Toll-like receptor 3 promotes cross-priming to virus-infected cells. *Nature* **433**, 887–892 (2005).
40. Jelinek, I. *et al.* TLR3-specific double-stranded RNA oligonucleotide adjuvants induce dendritic cell cross-presentation, CTL responses, and antiviral protection. *J.*

Immunol. **186**, 2422–2429 (2011).

41. Ko, K. H. *et al.* A novel defined TLR3 agonist as an effective vaccine adjuvant. *Front. Immunol.* **14**, 1075291 (2023).
42. Kang, D.-C. *et al.* mda-5: An interferon-inducible putative RNA helicase with double-stranded RNA-dependent ATPase activity and melanoma growth-suppressive properties. *Proc. Natl. Acad. Sci. U. S. A.* **99**, 637–642 (2002).
43. Yoneyama, M. *et al.* The RNA helicase RIG-I has an essential function in double-stranded RNA-induced innate antiviral responses. *Nat. Immunol.* **5**, 730–737 (2004).
44. De Waele, J. *et al.* A systematic review on poly(I:C) and poly-ICLC in glioblastoma: adjuvants coordinating the unlocking of immunotherapy. *J. Exp. Clin. Cancer Res.* **40**, 213 (2021).
45. Le Naour, J., Galluzzi, L., Zitvogel, L., Kroemer, G. & Vacchelli, E. Trial watch: TLR3 agonists in cancer therapy. *Oncoimmunology* **9**, 1771143 (2020).
46. Hafner, A. M., Corthésy, B. & Merkle, H. P. Particulate formulations for the delivery of poly(I:C) as vaccine adjuvant. *Adv. Drug Deliv. Rev.* **65**, 1386–1399 (2013).
47. Cao, L. *et al.* Design of protein-binding proteins from the target structure alone. *Nature* **605**, 551–560 (2022).
48. Chevalier, A. *et al.* Massively parallel de novo protein design for targeted therapeutics. *Nature* **550**, (2017).
49. Fleishman, S. J. *et al.* Computational design of proteins targeting the conserved stem region of influenza hemagglutinin. *Science* **332**, 816–821 (2011).
50. Silva, D. A. *et al.* De novo design of potent and selective mimics of IL-2 and IL-15. *Nature* **565**, (2019).
51. Chen, Y.-H., Lipes, B. D., Kenan, D. J., Staats, H. F. & Gunn, M. D. Identification of recombinant antibodies against multiple distinct toll-like receptors by homolog mining a single immune scFv phage library. *J. Immunol. Methods* **340**, 144–153 (2009).
52. Lipes, B. D. *et al.* An entirely cell-based system to generate single-chain antibodies against cell surface receptors. *J. Mol. Biol.* **379**, 261–272 (2008).
53. Dou, J. *et al.* De novo design of a fluorescence-activating β-barrel. *Nature* **561**, 485–491 (2018).
54. Lauer, T. M. *et al.* Developability index: a rapid in silico tool for the screening of antibody aggregation propensity. *J. Pharm. Sci.* **101**, 102–115 (2012).
55. Boder, E. T. & Wittrup, K. D. Yeast surface display for screening combinatorial polypeptide libraries. *Nat. Biotechnol.* **15**, 553–557 (1997).
56. Ishida, H. *et al.* Cryo-EM structures of Toll-like receptors in complex with UNC93B1. *Nat. Struct. Mol. Biol.* **28**, (2021).
57. Leonard, J. N. *et al.* The TLR3 signaling complex forms by cooperative receptor dimerization. *Proc. Natl. Acad. Sci. U. S. A.* **105**, 258–263 (2008).
58. Vavra, K. C., Xia, Y. & Rock, R. S. Competition between Coiled-Coil Structures and the Impact on Myosin-10 Bundle Selection. *Biophys. J.* **110**, 2517–2527 (2016).
59. Burdelya, L. G. *et al.* An agonist of toll-like receptor 5 has radioprotective activity in mouse and primate models. *Science* **320**, 226–230 (2008).
60. Komal, A., Noreen, M. & El-Kott, A. F. TLR3 agonists: RGC100, ARNAX, and

poly-IC: a comparative review. *Immunol. Res.* **69**, 312–322 (2021).
61. Mata-Haro, V. *et al.* The vaccine adjuvant monophosphoryl lipid A as a TRIF-biased agonist of TLR4. *Science* **316**, 1628–1632 (2007).
62. Frega, G. *et al.* Trial Watch: experimental TLR7/TLR8 agonists for oncological indications. *Oncoimmunology* **9**, 1796002 (2020).
63. Smirnov, D., Schmidt, J. J., Capecchi, J. T. & Wightman, P. D. Vaccine adjuvant activity of 3M-052: an imidazoquinoline designed for local activity without systemic cytokine induction. *Vaccine* **29**, 5434–5442 (2011).
64. Dempsey, P. W., Allison, M. E., Akkaraju, S., Goodnow, C. C. & Fearon, D. T. C3d of complement as a molecular adjuvant: bridging innate and acquired immunity. *Science* **271**, 348–350 (1996).
65. Melchers, M. *et al.* A stabilized HIV-1 envelope glycoprotein trimer fused to CD40 ligand targets and activates dendritic cells. *Retrovirology* **8**, 48 (2011).
66. Isik, G., Sliepen, K., van Montfort, T. & Sanders, R. W. Enhanced immunogenicity of HIV-1 envelope gp140 proteins fused to APRIL. *PLoS One* **9**, e107683 (2014).
67. Song, L. *et al.* Superior efficacy of a recombinant flagellin:H5N1 HA globular head vaccine is determined by the placement of the globular head within flagellin. *Vaccine* **27**, 5875–5884 (2009).
68. Huleatt, J. W. *et al.* Vaccination with recombinant fusion proteins incorporating Toll-like receptor ligands induces rapid cellular and humoral immunity. *Vaccine* **25**, 763–775 (2007).
69. Scheerlinck, J. Y. Genetic adjuvants for DNA vaccines. *Vaccine* **19**, 2647–2656 (2001).
70. Tse, S.-W. *et al.* mRNA-encoded, constitutively active STINGV155M is a potent genetic adjuvant of antigen-specific CD8+ T cell response. *Mol. Ther.* **29**, 2227–2238 (2021).
71. Lu, Y. & Swartz, J. R. Functional properties of flagellin as a stimulator of innate immunity. *Sci. Rep.* **6**, (2016).
72. Song, L. *et al.* Enhanced immunogenicity elicited by a novel DNA vaccine encoding the SARS-CoV-2 S1 protein fused to the optimized flagellin of Salmonella typhimurium in mice. *Microbiol Spectr* **11**, e0254923 (2023).
73. Rady, H. F., Dai, G., Huang, W., Shellito, J. E. & Ramsay, A. J. Flagellin Encoded in Gene-Based Vector Vaccines Is a Route-Dependent Immune Adjuvant. *PLoS One* **11**, e0148701 (2016).
74. Yu, M. & Levine, S. J. Toll-like receptor, RIG-I-like receptors and the NLRP3 inflammasome: key modulators of innate immune responses to double-stranded RNA viruses. *Cytokine Growth Factor Rev.* **22**, 63–72 (2011).
75. Pichlmair, A. *et al.* RIG-I-mediated antiviral responses to single-stranded RNA bearing 5’-phosphates. *Science* **314**, 997–1001 (2006).
76. Tenthorey, J. L. *et al.* The structural basis of flagellin detection by NAIP5: A strategy to limit pathogen immune evasion. *Science* **358**, 888–893 (2017).
77. Shi, J. *et al.* Inflammatory caspases are innate immune receptors for intracellular LPS. *Nature* **514**, 187–192 (2014).
78. Wagner, H. & Bauer, S. All is not Toll: new pathways in DNA recognition. *J. Exp. Med.* **203**, 265–268 (2006).

79. Querec, T. *et al.* Yellow fever vaccine YF-17D activates multiple dendritic cell subsets via TLR2, 7, 8, and 9 to stimulate polyvalent immunity. *J. Exp. Med.* **203**, 413–424 (2006).
80. Kim, J. H. *et al.* Crystal structures of mono- and bi-specific diabodies and reduction of their structural flexibility by introduction of disulfide bridges at the Fv interface. *Sci. Rep.* **6**, 1–12 (2016).
81. Langan, R. A. *et al.* De novo design of bioactive protein switches. *Nature* **572**, 205–210 (2019).
82. Mohan, K. *et al.* Topological control of cytokine receptor signaling induces differential effects in hematopoiesis. *Science* **364**, (2019).
83. Watson, J. L. *et al.* De novo design of protein structure and function with RFdiffusion. *Nature* **620**, 1089–1100 (2023).
84. Schneidman-Duhovny, D., Inbar, Y., Nussinov, R. & Wolfson, H. J. PatchDock and SymmDock: servers for rigid and symmetric docking. *Nucleic Acids Res.* **33**, W363 (2005).
85. Silva, D.-A., Correia, B. E. & Procko, E. Motif-Driven Design of Protein–Protein Interfaces. in *Computational Design of Ligand Binding Proteins* (ed. Stoddard, B. L.) 285–304 (Springer New York, New York, NY, 2016).
86. Zhang, J., Kobert, K., Flouri, T. & Stamatakis, A. PEAR: a fast and accurate Illumina Paired-End reAd mergeR. *Bioinformatics* **30**, 614–620 (2013).
87. Studier, F. W. Stable expression clones and auto-induction for protein production in E. coli. *Methods Mol. Biol.* **1091**, 17–32 (2014).
88. Jacobs, T. M., Yumerefendi, H., Kuhlman, B. & Leaver-Fay, A. SwiftLib: rapid degenerate-codon-library optimization through dynamic programming. *Nucleic Acids Res.* **43**, e34 (2015).
89. Han, Y. *et al.* High-yield monolayer graphene grids for near-atomic resolution cryoelectron microscopy. *Proc. Natl. Acad. Sci. U. S. A.* **117**, 1009–1014 (2020).
90. Sun, M. Practical considerations for using K3 cameras in CDS mode for high-resolution and high-throughput single particle cryo-EM. *J. Struct. Biol.* **213**, (2021).
91. Zheng, S. Q. MotionCor2: anisotropic correction of beam-induced motion for improved cryo-electron microscopy. *Nat. Methods* **14**, (2017).
92. Rohou, A. & Grigorieff, N. CTFFIND4: Fast and accurate defocus estimation from electron micrographs. *J. Struct. Biol.* **192**, (2015).
93. Punjani, A., Rubinstein, J. L., Fleet, D. J. & Brubaker, M. A. cryoSPARC: algorithms for rapid unsupervised cryo-EM structure determination. *Nat. Methods* **14**, (2017).
94. Punjani, A., Zhang, H. & Fleet, D. J. Non-uniform refinement: adaptive regularization improves single-particle cryo-EM reconstruction. *Nat. Methods* **17**, (2020).
95. Rubinstein, J. L. & Brubaker, M. A. Alignment of cryo-EM movies of individual particles by optimization of image translations. *J. Struct. Biol.* **192**, (2015).
96. Zivanov, J., Nakane, T. & Scheres, S. H. W. Estimation of high-order aberrations and anisotropic magnification from cryo-EM data sets in RELION-3.1. *IUCrJ* **7**, 253–267 (2020).
97. Rosenthal, P. B. & Henderson, R. Optimal determination of particle orientation,

absolute hand, and contrast loss in single-particle electron cryomicroscopy. *J. Mol. Biol.* **333**, (2003).

98. Kucukelbir, A., Sigworth, F. J. & Tagare, H. D. Quantifying the local resolution of cryo-EM density maps. *Nat. Methods* **11**, (2014).
99. Sanchez-Garcia, R. *et al.* DeepEMhancer: a deep learning solution for cryo-EM volume post-processing. *Commun Biol* **4**, 874 (2021).
100. Emsley, P. & Cowtan, K. Coot: model-building tools for molecular graphics. *Acta Crystallogr. D Biol. Crystallogr.* **60**, (2004).
101. Poirot, O., O'Toole, E. & Notredame, C. Tcoffee@igs: A web server for computing, evaluating and combining multiple sequence alignments. *Nucleic Acids Res.* **31**, 3503–3506 (2003).
102. Hayashi, F. *et al.* The innate immune response to bacterial flagellin is mediated by Toll-like receptor 5. *Nature* **410**, 1099–1103 (2001).
103. Mizel, S. B. & Bates, J. T. Flagellin as an Adjuvant: Cellular Mechanisms and Potential. *J. Immunol.* **185**, 5677 (2010).
104. Smith, K. D. *et al.* Toll-like receptor 5 recognizes a conserved site on flagellin required for protofilament formation and bacterial motility. *Nat. Immunol.* **4**, 1247–1253 (2003).
105. Il Kim, M., Lee, C., Park, J., Jeon, B.-Y. & Hong, M. Crystal structure of Bacillus cereus flagellin and structure-guided fusion-protein designs. *Sci. Rep.* **8**, 1–10 (2018).
106. Mark A.B. Kreutzberger, Ravi R. Sonani, Junfeng Liu, Sharanya Chatterjee, Fengbin Wang, Amanda L. Sebastian, Priyanka Biswas, Cheryl Ewing, Weili Zheng, Frédéric Poly, Gad Frankel, B.F. Luisi, Chris R. Calladine, Mart Krupovic, Birgit E. Scharf, Edward H. Egelman. Convergent evolution in the supercoiling of prokaryotic flagellar filaments. *Cell* **185**, 3487–3500.e14 (2022).
107. Lu, Y., Welsh, J. P., Chan, W. & Swartz, J. R. Escherichia coli-based cell free production of flagellin and ordered flagellin display on virus-like particles. *Biotechnology and Bioengineering* vol. 110 2073–2085 Preprint at https://doi.org/10.1002/bit.24903 (2013).
108. Dauparas, J. *et al.* Robust deep learning-based protein sequence design using ProteinMPNN. *Science* **378**, 49–56 (2022).
109. Song, W. S., Jeon, Y. J., Namgung, B., Hong, M. & Yoon, S.-I. A conserved TLR5 binding and activation hot spot on flagellin. *Sci. Rep.* **7**, 1–11 (2017).
110. Recombinant expression of TLR5 proteins by ligand supplementation and a leucine-rich repeat hybrid technique. *Biochem. Biophys. Res. Commun.* **427**, 119–124 (2012).
111. Sumida, K. H. *et al.* Improving Protein Expression, Stability, and Function with ProteinMPNN. *J. Am. Chem. Soc.* (2024) doi:10.1021/jacs.3c10941.
112. Lee, E. B. *et al.* Attachment of flagellin enhances the immunostimulatory activity of a hemagglutinin-ferritin nano-cage. *Nanomedicine* **17**, (2019).
113. Wang, C., Zhu, W. & Wang, B. Z. Dual-linker gold nanoparticles as adjuvanting carriers for multivalent display of recombinant influenza hemagglutinin trimers and flagellin improve the immunological responses in vivo and in vitro. *Int. J. Nanomedicine* **12**, (2017).

114. Walls, A. C. *et al.* Elicitation of Potent Neutralizing Antibody Responses by Designed Protein Nanoparticle Vaccines for SARS-CoV-2. *Cell* **183**, (2020).
115. Bale, J. B. *et al.* Accurate design of megadalton-scale two-component icosahedral protein complexes. *Science* **353**, 389–394 (2016).
116. Qiao, Y. *et al.* Pam2CSK4-adjuvanted SARS-CoV-2 RBD nanoparticle vaccine induces robust humoral and cellular immune responses. *Front. Immunol.* **13**, (2022).
117. Dang, B. *et al.* De novo design of covalently constrained mesosize protein scaffolds with unique tertiary structures. *Proc. Natl. Acad. Sci. U. S. A.* **114**, 10852–10857 (2017).
118. Klesney-Tait, J., Turnbull, I. R. & Colonna, M. The TREM receptor family and signal integration. *Nat. Immunol.* **7**, 1266–1273 (2006).
119. Tammaro, A. *et al.* TREM-1 and its potential ligands in non-infectious diseases: from biology to clinical perspectives. *Pharmacol. Ther.* **177**, 81–95 (2017).
120. Zhong, L. *et al.* TREM2/DAP12 Complex Regulates Inflammatory Responses in Microglia via the JNK Signaling Pathway. *Front. Aging Neurosci.* **9**, 204 (2017).
121. Nakamura, K. & Smyth, M. J. TREM2 marks tumor-associated macrophages. *Signal Transduct Target Ther* **5**, 233 (2020).
122. Jay, T. R., von Saucken, V. E. & Landreth, G. E. TREM2 in Neurodegenerative Diseases. *Mol. Neurodegener.* **12**, 56 (2017).
123. Molgora, M. *et al.* TREM2 Modulation Remodels the Tumor Myeloid Landscape Enhancing Anti-PD-1 Immunotherapy. *Cell* **182**, 886–900.e17 (2020).
124. Rapaka, R. R., Cross, A. S. & McArthur, M. A. Using Adjuvants to Drive T Cell Responses for Next-Generation Infectious Disease Vaccines. *Vaccines* **9**, (2021).
125. Bournazos, S., Corti, D., Virgin, H. W. & Ravetch, J. V. Fc-optimized antibodies elicit CD8 immunity to viral respiratory infection. *Nature* **588**, 485–490 (2020).
126. Nimmerjahn, F. & Ravetch, J. V. Fcγ receptors as regulators of immune responses. *Nat. Rev. Immunol.* **8**, 34–47 (2008).
127. Fridman, W. H. Fc receptors and immunoglobulin binding factors1. *The FASEB Journal* **5**, 2684–2690 (1991).
128. Patel, K. R., Roberts, J. T. & Barb, A. W. Multiple Variables at the Leukocyte Cell Surface Impact Fc γ Receptor-Dependent Mechanisms. *Front. Immunol.* **10**, 223 (2019).
129. Junker, F., Gordon, J. & Qureshi, O. Fc Gamma Receptors and Their Role in Antigen Uptake, Presentation, and T Cell Activation. *Front. Immunol.* **11**, (2020).
130. Overview of Fc Receptors: classification and functions - ACROBiosystems. https://acrobiosystems.com.cn/A1341-Overview-of-Fc-Receptors%3A-classification-and-functions.html.
131. Clarke, C. Computational Design of Proteins that Bind to TLR7 and FCyRIIa. (2023).
132. Yamin, R. *et al.* Fc-engineered antibody therapeutics with improved anti-SARS-CoV-2 efficacy. *Nature* **599**, 465–470 (2021).
133. Sahtoe, D. D. *et al.* Reconfigurable asymmetric protein assemblies through implicit negative design. *Science* **375**, (2022).